1

Two-dimensional Transition Metal Dichalcogenides: A General Overview

Chi Sin Tang[1,2] and Xinmao Yin[2]

[1] National University of Singapore, Singapore Synchrotron Light Source (SSLS), 5 Research Link, Singapore, 117603, Singapore
[2] Shanghai University, Shanghai Key Laboratory of High Temperature Superconductors, Shanghai Frontiers Science Center of Quantum and Superconducting Matter States, Physics Department, 99 Shangda Road, Shanghai 200444, China

1.1 Introduction to 2D-TMDs

Since graphene was first exfoliated from graphite using the mechanical cleavage method [1], 2D materials have garnered widespread interest. Atomically thin 2D-TMDs, with a formula of MX_2 (M: transition metal atom; X: chalcogen atom), form a diverse class of 2D materials with about 60 members. While one can trace back the extensive studies on bulk and multilayer TMD materials to more than half a century ago [2], it was only the groundbreaking emergence of graphene of single-atom thickness [1, 3] that led to the tremendous progress of monolayer van der Waals systems within the last two decades. With unique optoelectronic properties and robust mechanical features, 2D-TMD is a class of low-dimensional materials ideal for multiple applications in areas such as electronics, optoelectronics, and valleytronics [4–6]. They surpass graphene in terms of their functionality due to the combination of their non-zero bandgap electronic structures and their pristine yet robust layered surface properties. 2D-TMD is also a favorable class of materials in practical applications related to field-effect-transistor (FET) based systems. Hence, extensive research studies have taken center stage over the past decade to uncover both the fundamental physical properties and to unleash new frontiers for possible 2D-TMD-based device applications.

At the molecular level, diverse variations to the chemical bonding and crystal configurations of the transition metal atom component in 2D-TMDs have led to multiple structural phases that possess unique electronic properties. The semiconducting 1H phase is a quintessential example. Structural changes to one of the chalcogen planes will result in the metallic 1T phase. In addition, a unique quasi-metallic 1T'phase arises due to its distorted sandwich structure, where an array of one-dimensional zigzag transition metal chains are formed [7, 8].

Two-Dimensional Transition-Metal Dichalcogenides: Phase Engineering and Applications in Electronics and Optoelectronics, First Edition. Edited by Chi Sin Tang, Xinmao Yin, and Andrew T. S. Wee.

1.2 Crystal Structures of 2D-TMDs in Different Phases

TMDs present various structural polymorphs which have attracted huge interest in the last decade, both as an ideal platform for the fundamental study of layered quantum systems and their potential for multiple applications. Structurally, a unit layer is made up of a transition metal layer sandwiched between two chalcogen layers. Interestingly, TMDs, whether in the mono or multi-layer form, manifest themselves in different structural phases arising due to different configurations of the transition metal atom component. The common polymorphs of 2D-TMDs are the trigonal prismatic 1H phase and the octahedral 1T phase. In the case of the octahedral 1T phase structure, it has been experimentally and theoretically shown that it is dynamically unstable under free-standing conditions [7–9]. Consequently, similar to the Peierls distortion, the 1T phase will relax and buckle spontaneously into a thermodynamically more stable distorted structure known as the 1T′ phase [7–9]. Hence, 1T phase 2D-TMDs can further stabilize under favorable chemical, thermal and mechanical conditions [10], particularly into the 1T′phase.

To better understand the diverse structural properties of 2D-TMDs, the respective structural phases can be visualized by the stacking configurations of the three atomic planes (i.e. the X-M-X structure). The 1H phase corresponds to an ABA stacking configuration where the chalcogen atoms at the top and bottom atomic planes are in the same vertical position and are located on top of each other in a direction perpendicular to the layer (Figure 1.1a). In contrast, the 1T structural phase has an ABC stacking configuration displayed in Figure 1.1b. Since the 1T phase structure is unstable under freestanding conditions, it will buckle and distort into the 1T′ structure where the transition metal atoms sandwiched between the upper and lower atomic layers distort. Consequently, it forms a period doubling 2×1 structure. As viewed from the top, this structural phase consists of an array of 1D zigzag transition metal chains (Figure 1.1c). Indeed, recent investigations related to symmetry-reducing CDW properties [12] in metallic 1T phase 2D-TMDs have created new opportunities for integrated low-dimensional material-based applications, including transistor systems, nanoscale charge channels and gate switching devices [13–15]. Besides, 1T′ phase 2D-TMDs are known to possess anisotropic electronic and optical features. An in-depth understanding of its unique structure can bring new insights to its characteristics, which can then be exploited for directionally regulated charge or photon channel applications in optoelectronics and electronics.

As discussed thereafter, electronic structure calculations have indicated that while the 1T phase 2D-TMD is metallic [10, 16], the 1T′ phase counterpart possesses a unique quasi-metallic electronic structure that will be discussed later. To clearly distinguish between these two structural phases, note that while low-temperature charge density wave (CDW) phases are typically observed in 1T phase TMD systems (e.g. T_{CDW} ~120 K for $TaSe_2$ and T_{CDW}~35 K for $NbSe_2$ [17, 18]), a CDW-like lattice distortion in the form of periodic 1D zigzag chain structure unique to the 1T′phase 2D-TMD can be observed even at room temperature [7, 8]. Morphologically, while the low-temperature commensurates CDW in 1T phase, TMDs can be distinguished

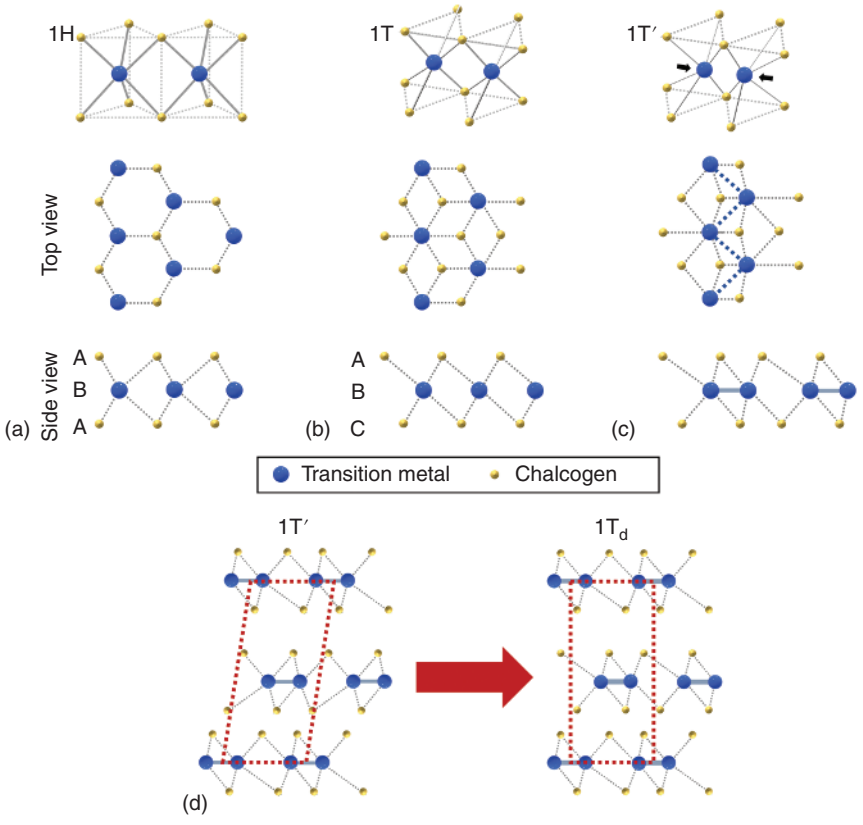

Figure 1.1 Lattice structures of 2D-TMDs in the (a) trigonal prismatic (1H), (b) octahedral (1T), and (c) distorted (1T′) phases. Stacking configuration of the atomic planes have been indicated. (d) The stacking orders that distinguish between the 1T′ and the 1T$_d$ phases. The red dashed boxes serve as visual guides. Source: Tang et al. [11]/With permission of AIP Publishing.

by a unique star-of-David superlattice [19–21] typically characterized using scanning tunneling microscopy. Conversely, the 1D zigzag chains in the 1T′ phase are clearly distinguished via high-resolution transmission electron microscopy.

1.2.1 Other Structural Phases

Apart from the three common structural phases, TMDs are also present in other structural phases each with their unique optical and electronic properties. For example, $MoTe_2$ and WTe_2 would undergo a first-order phase transition from the monoclinic 1T′ phase to form the orthogonal $1T_d$ phase as temperature decreases. While the structures of both the 1T′ and $1T_d$ phase are rather similar, their key differences lie with the dislocations between the stacking layers depicted in the layer distortion in Figure 1.1d. These seemingly trivial dislocations can lead to a significant symmetry change between the two structural phases [22, 23]. Nevertheless,

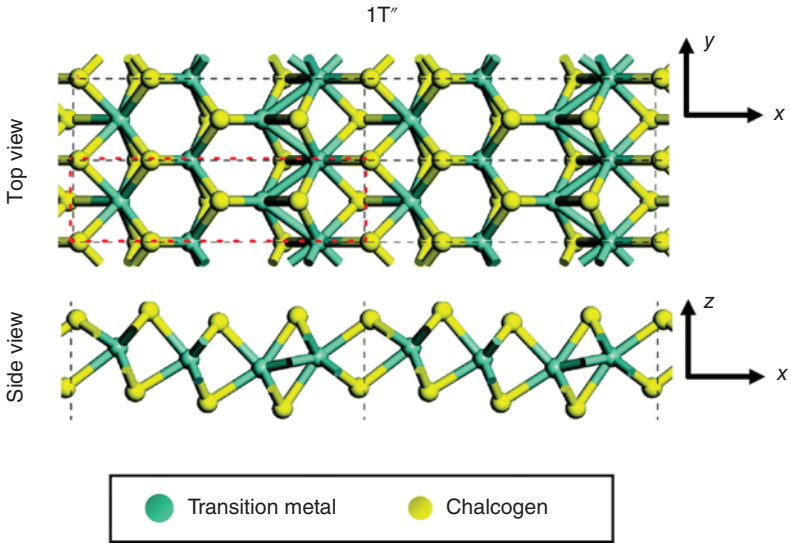

Figure 1.2 Atomic structures of the 1T″-phase 2D-TMD with the atomic planes indicated. Source: Reproduced with permission from Ma et al. [24]. Copyright 2016, The Royal Society of Chemistry.

with a similar structure present in the respective layer, $1T_d$ phase TMDs still possess similar quasi-metallic electronic properties as that of its 1T′ phase counterparts [9, 22, 23].

In the monolayer regime, apart from the formation of the 1T′ structural phase due to distortion from its 1T phase counterpart, other stable polymorphs have also been reported. This includes another octahedrally coordinated 1T″ phase (Figure 1.2) [25]. While there is an association between the transition metal atoms in the M–M configuration in the 1T′ and 1T″ distorted phases, the transition metal atoms are dimerized in the 1T′ phase while trimerization takes place in the 1T″ phase [26]. Besides, while the 1T′ phase possesses quasi-metallic electronic properties, computational studies have suggested that the 1T″ phase is a wide bandgap semiconductor where 1T″ phase monolayer-MoS_2 possesses an indirect bandgap of ~0.27 eV [24]. Nevertheless, no consensus has been reached in terms of the relative stability between the octahedral phases, particularly for monolayer-MoS_2, where different studies have reported different stability levels between the structural phases [24, 27, 28].

1.2.2 Phase Stability

Theoretical studies have shown that the 1H-1T′ energy differences vary between different Mo- and W-based 2D-TMD species, especially with the inclusion of spin-orbit coupling [29, 30]. Figure 1.3 displays the phase energetics of the respective monolayers in their respective phases as extracted from Ref. [30, 31], with $U = 0$ as the reference energy for the respective 2D-TMD in their 1H phase and 1T phase, which

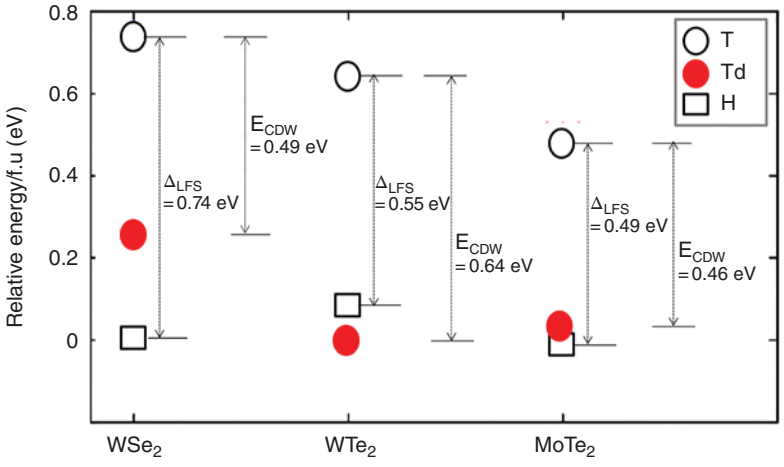

Figure 1.3 Relative stability of various phases of TMDs in the H, T, and T_d structural phases. The zero energy is the most stable phase for the TMDs. Source: Reproduced with permission from Santhosh et al. [31] © 2015 IOP Publishing Ltd.

are the most unstable of the polymorph. A smaller energy difference between the 1T′ and the 1H phase would mean a correspondingly smaller amount of external energy required to induce the 1H-1T′ phase transition. In the case of monolayer-WTe_2, the $U < 0$ registered for the 1T′ phase suggests that the compound is more stable in its 1T′ phase — i.e. 1H-1T′ phase transition takes place spontaneously without any external influence.

Even in the case of phase stability between the 1H and 1T phases, multiple studies have already been conducted specifically for $MoTe_2$ [32]. Under more general circumstances, simulations that involve the stability of different 2D-TMD species have also been extensively studied with a summary comprising 44 species displayed in Figure 1.4 [33]. When in their respective ground state polymorph, their different 2D-TMD species can possess semiconducting (T**/H**), metallic (T*/H*), or half-metallic (T^+) behaviors.

Based on the energy differences between the semiconducting 1H and quasi-metallic 1T′ phase of the respective Mo and W-based 2D-TMDs, the application of different electrostatic gating configurations can drive their 1H-1T′ phase transition. This is carried out by changing the carrier density or electron-chemical potential in the monolayer-TMD via a capacitor structure displayed in Figure 1.5 [29]. Specifically, in the case of undoped monolayer-$MoTe_2$ with a very small energy difference between the 1H and 1T′ phases, a mere surface charge density below $-0.04e$ or above $+0.09e$ per unit cell is required to drive the 1H-1T′ structural phase transition under pristine conditions. Whereas a significantly higher surface charge density of about $-0.29e$ or above $+0.35e$ per unit cell is required to drive the same structural transition for monolayer-MoS_2.

The control of pressure is a thermodynamic parameter that affects the phase stability of 2D-TMDs and induces a structural phase transition. As mentioned

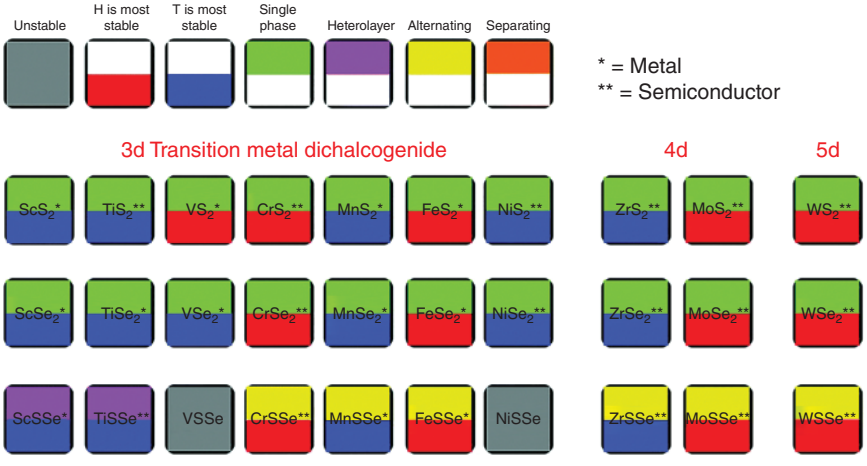

Figure 1.4 The structural stability and the electronic properties single phase and mixed phase of TMDs summarized in the table. The transition-metal atomic components are classified into the 3d, 4d, and 5d groups. With the gray colour boxes indicating phase separation. The resulting structural phases (T or H) could be metallic (*) or semiconducting (**). Source: Reproduced with permission.

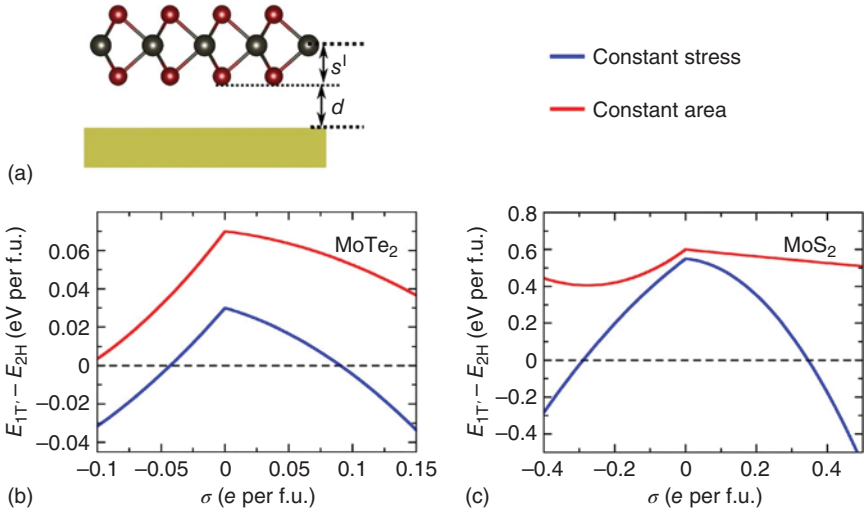

Figure 1.5 Phase boundary under constant charge in $MoTe_2$ and MoS_2 monolayers. (a) Schematic of a monolayer TMD lattice and an electron reservoir such as a metallic surface that is separated by a vacuum layer. Evolution in the energy difference of the respective 2D-TMDs between their 1H and 1T′ phases changes with respect to charge density, σ. The blue line represents situations where both the 1H and 1T′-phase lattices are in relaxed state while the red line represents the constant-area case where monolayer is kept to the area when under 1H-phase lattice constants. (b) 1H-phase $MoTe_2$ is a stable phase while 1T′-phase $MoTe_2$ is metastable when the monolayer is charge neutral. However, 1T′-phase $MoTe_2$ becomes increasingly stable when charged beyond the positive or negative threshold values. (c) 1H-phase monolayer-MoS_2 is stable when charge neutral. Nevertheless, the magnitude of charge required to induce 1H-1T′ transition is larger than its $MoTe_2$ counterpart. In both cases, transition at constant stress is more easily induced than the transition under constant area. Source: Li et al. [29]/Springer Nature/Licensed under CC BY 4.0.

earlier, the highly symmetric 1T phase structure for Mo and W-based 2D-TMDs is unstable under free-standing conditions and ambient pressure. They will therefore buckle and convert readily to the octahedral-like 1T′ phase structure. Density functional theory (DFT)- based studies to determine the phase diagrams of 2D-TMD with respect to tensile strain have shown that to maintain the stability of the metallic 1T phase structure, an equi-biaxial tensile strain of 10–15% is required for most 2D-TMDs (e.g. 13% for monolayer-MoS_2) except for $MoTe_2$. For the latter, a considerably smaller tensile strain <1.5% is required under appropriate constraints [30]. Given the small energy differences between the 1H and 1T′ phases for $MoTe_2$, minimal temperature changes also have profound effects on the transition dynamics due to the introduction of vibration effects to the system. Hence, the strain required to induce the structural phase transition is reduced at elevated temperatures [30]. Even monolayer-WTe_2, which is energetically more stable in the 1T′ phase under pristine conditions, will transform into semiconducting 1H phase when lattice compression is applied.

It is further discovered that the coexistence of multiple phases within a system – easily achievable under laboratory settings – is thermodynamically stable under reasonable thermodynamic conditions. Experimentally, such studies are achievable with a certain degree of restrictions. While tensile strain can easily be applied to 2D-TMDs by attaching it to a large elastic substrate where its deformations can be regulated [34, 35], the spontaneous formation of ripple patterns complicates the strain process and characterization [35–37]. As for bulk or multi-layer materials, deformations that are sufficiently significant can only be achieved via compression processes.

1.3 Electronic Band Structures of 2D-TMDs

Given the number of members in the 2D-TMD family, they exhibit a diverse range of macro properties related to their mechanical and electronic features. Their properties also differ between the monolayer, multilayer, and bulk counterparts. For example, in their bulk form, niobium, tantalum-based sulfides, and selenides as well as β-$MoTe_2$, and $1T_d$ phase WTe_2 possess metallic properties [38–41]. Conversely, TMD species such as the commonly studied MoS_2, WS_2, $MoSe_2$, WSe_2, α-$MoTe_2$, ReS_2, and ZrS_2 are semiconducting in nature [38, 39, 42–44]. At the molecular level, the interlayer van der Waals forces of interaction play a pivotal role in dictating their properties at both the macro and micro-electronic level. Even at the intralayer level, the intrinsic interactions taking place between the constituent atoms play a critical role in dictating the properties of the TMD species. Therefore, even though the lattice structures of the respective phases may be similar for different 2D-TMDs, the extensive interplay of the spin, charge, and orbital degrees of freedom result in very distinct electronic and optoelectronic properties.

In addition, apart from the chemical compositions of different 2D-TMDs, the diversity of structural phases and their respective stabilities brings about unique optoelectronic properties because of their unique electronic band structure, and

the emergence of novel correlated and topological phases. These polymorphic electronic features are intimately related to the coupling between their charge, spin, orbital, and lattice degrees of freedom. A distinct example to be further elaborated on would be the presence of strong spin-orbit coupling that leads to the opening of the fundamental gap in 1T′ phase 2D-TMDs [8, 9].

1.3.1 Electronic Band Structures of the 1H, 1T, and 1T′ Phase

The electronic band structures of 2D-TMDs are dictated by multiple effects including strong Coulomb interaction between the constituent atoms and the effects of crystal symmetry. Meanwhile, spin-orbital coupling also has their distinct roles in determining the unique orbital characters, spin-valley properties, and unique optical selection rules. As discussed in the following section, the electronic band structures of multilayer TMD systems in the 2H-phase are a result of the weak interlayer van der Waals interactions. Structurally, 2H phase layered TMDs are characterized by the D_{6h} point symmetry group [45, 46]. Unlike their monolayer (1H) counterparts (Figure 1.6a), 2H phase multilayer and bulk TMDs are indirect bandgap semiconductors where the valence band maximum (VBM) is situated at the Γ-point of the hexagonal Brillouin zone, while the conduction band minimum (CBM) is approximately halfway between the Γ- and K-points (Figure 1.6b) [48, 49].

When examined in greater detail, by taking the example of monolayer-WSe_2 with spin-orbit coupling accounted for, the electronic bands at the Γ-point consist of contributions from both the Se (chalcogen) p_z-orbitals and the (transition mtal) d_{z^2}-orbitals in both the valence and conduction bands (Figures 1.7a,b, respectively). The energy bands of both the conduction and valence bands at the K/K'-points have a majority in-plane contribution from the localized transition metal orbitals. They include the $d_{x^2-y^2}$, and id_{xy}-states (VB) and a mixture of both the $mtald_{z^2}$ and chalcogen $p_x \mp ip_y$ orbitals at the conduction band [50–52]. The spatial overlap between adjacent layers and their corresponding effects on the band structure has

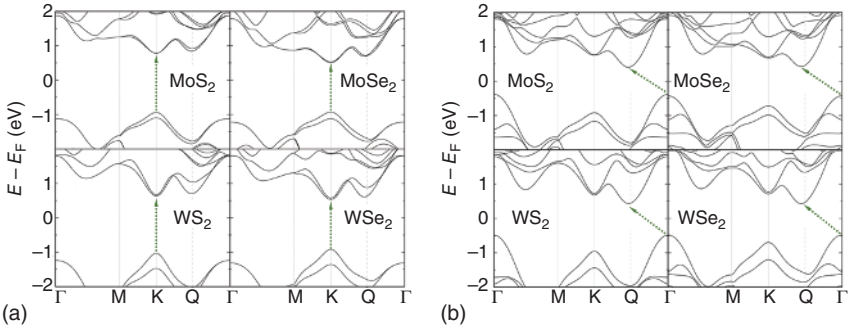

Figure 1.6 Comparing the band structures of the respective TMD materials in their monolayer and bulk form with SOC accounted for. (a) Band structure of MoS_2, $MoSe_2$, WS_2, and WSe_2 monolayers obtained from DFT calculations. Dashed arrows suggest that these are direct bandgap semiconductors. (b) Band structure of bulk MoS_2, $MoSe_2$, WS_2, and WSe_2 obtained from DFT calculations. Dashed arrows suggest that these are indirect bandgap semiconductors in their bulk form. Source: Roldán et al. [47]/With permission of John Wiley & Sons.

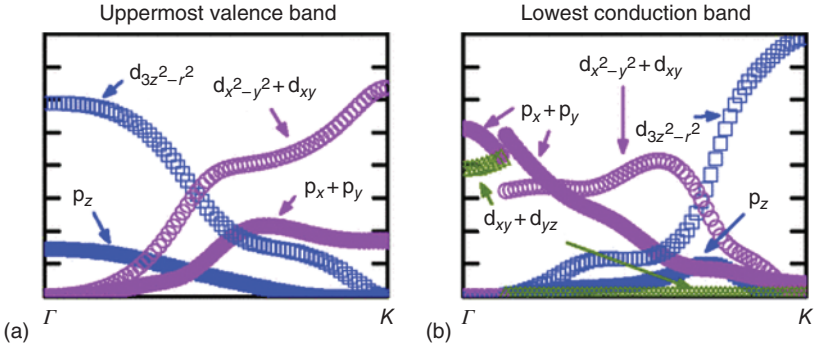

Figure 1.7 Spin-splitting in the valence and conduction bands as functions of $k_{//}$ along the $\Gamma-K$ points in the Brillouin zone with the contributions of the W (*d*) and Se (*p*) orbitals. (a) Uppermost valence band, and (b) lowermost conduction band. Source: Zhu et al. [50]/With permission of American Physical Society.

long-standing effects with variable layer thickness down to the monolayer limit [53, 54].

As for the electronic band structures of the commonly observed 1H, 1T, and 1T′ polymorphs, examples of the respective polymorphs of monolayer-MoS_2 are displayed in Figures. 1.8a,b,c, respectively [8, 54, 55]. The 1H-phase is a direct K–K bandgap semiconductor. The direct K–K transition has strong contributions from the transition metal d-orbitals (i.e. the Mo-atoms). With two contributing electrons from the transition metal d-orbitals, they will be paired and fully occupied in its lowest d_{z^2}-orbital state due to the hexagonal symmetry of the 1H phase structure. Hence, the 1H phase semiconducting structure is stabilized by the electron count of the transition metal d-orbitals. As discussed later, high-resolution scanning tunneling spectroscopy (STS) serves as an effective characterization technique that reveals a ∼2.4 eV bandgap for chemical vapor deposition (CVD) synthesized monolayer-MoS_2 where it has been demonstrated that this bandgap decreases significantly with increasing thickness [57]. The thickness-dependent band structures have been further characterized using high-resolution angle-resolved photoemission spectroscopy (ARPES) as displayed in Figure 1.8d,g [56]. Note how the electronic structures of MoS_2 near the Fermi level evolves between its mono-, bi-, trilayer and its bulk form [56].

In terms of the quasi-stable metallic 1T-phase, there is a degeneracy in the electronic structure (lowest $d_{xy,yz,zx}$ degenerate orbitals) that is attributed to the structure's tetragonal symmetry. This results in the partially occupied transition metal d-orbitals that brings about the metallic character. In the regions near the Γ-point, the Fermi-level crosses both the Mo d- and S p-orbitals (Figure 1.8b). While the 1H-phase structure is stabilized by the electron count of the transition metal d-orbitals, charge-doping processes such as intercalation, alloying, gating, and defect engineering processes are expected to modify the transition metal d-orbital electron population. Consequently, this de-stabilizes the 1H-phase structure and leads to a structural transition into the 1T or 1T′-phase. Apart from modifying the electron count, external effects in the form of atomic distortion can also destabilize

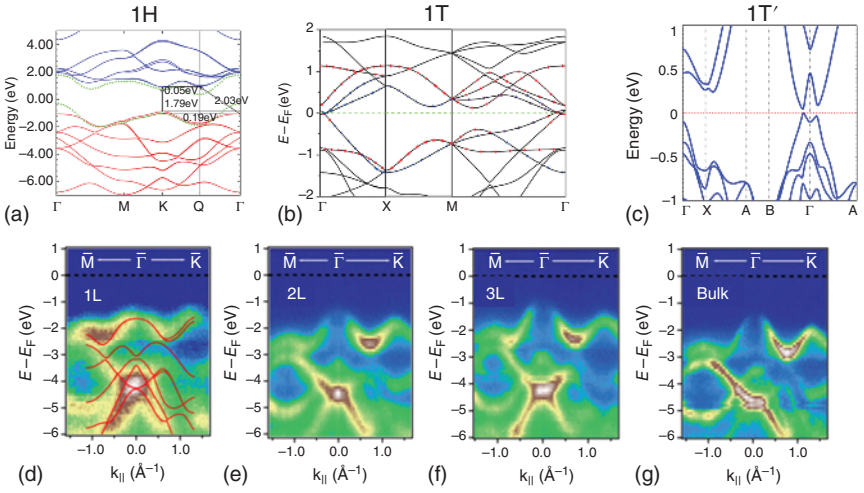

Figure 1.8 Theoretically and experimentally determined band structures of 2D-TMDs in their respective phases. (a) 1H, (b) 1T, and (c) 1T′-phase monolayer-MoS_2. The green lines in (a) show the top (bottom) valence (conduction) bands in bulk MoS_2. The lines marked by red and blue in (b) represent the bands, contributed mainly by the Mo 4d-orbitals and S 3p-orbitals, respectively. Band structure of 1T′-phase monolayer-MoS_2 in (c) with the fundamental, E_g, and inverted gap, 2δ. Inset: comparison of band structures with (red dashed line) and without (black solid line) spin-orbit coupling. ARPES band map of exfoliated (d) monolayer, (e) bilayer, (f) trilayer, and (g) bulk MoS_2 along the $M-\Gamma-K$ high symmetry lines. Source: (a) Kadantsev et al. [16]/Reproduced with permission from Elsevier. (b) Hu et al. [55]/Reproduced with permission from AIP Publishing. (c) Zhuang et al. [28]/Reproduced with permission of American Physical Society. (d)–(g) Reprinted with permission from Jin et al. [56], 2017 American Physical Society.

the electronic structure of the semiconducting 1H-phase which in turn leads to the formation of the 1T/1T′-phase.

As for the 1T′-phase 2D-TMDs, the zigzag chain structure lowers the transition metal d-orbitals below the chalcogen p-orbitals. This leads to a band inversion which in turn, leads to the formation of an inverted gap, 2δ, at the Γ-point in the Brillouin zone, along with two Dirac cones near the Γ-point in the 2D Brillouin zone. Under the influence of spin-orbit coupling, there is an opening of a fundamental gap, E_g, at the Dirac points (Figure 1.8(c)). ARPES study of 1T′-phase monolayer-WSe_2 synthesized by molecular beam epitaxy (MBE)[[58]] has shown a ~0.12 eV fundamental gap that is consistent with their band structure calculations. In this case the high-symmetry $\Gamma-Y$ and $\Gamma-P$ directional contributions have been detected in a single ARPES measurement. The STS and ARPES results exhibit the direct observation of the ~56 meV fundamental gap for the epitaxially grown 1T′-phase monolayer-WTe_2 [59]. Optical techniques have also been utilized to probe the optoelectronic properties of TMD materials. For instance, Fourier-transform infrared spectroscopy (FTIR) investigations by Keum et al. revealed an absorption feature at ~0.06 eV, which can be attributed to the fundamental gap of mechanically exfoliated 1T′-phase monolayer-$MoTe_2$ samples [9]. As presented later in the subsequent sections, spectroscopic ellipsometry has been used to probe the 1T′-phase MoS_2 and WSe_2 monolayers, where the emergence of the fundamental and inverted gaps has been observed [60, 61].

TMD systems in both their monolayer and multilayer forms exhibit myriads of rich physical phenomena, and they hold immense promise both in the realm of fundamental science and for future device and optoelectronic applications in their respective polymorphs. To effectively investigate and exploit the unique properties of each polymorph, efficient phase engineering strategies must be implemented to access the respective phases with minimal damage and interference to the system. The subsequent section will discuss the development of multiple phase transition strategies alongside the challenges and advantages each of them hold.

1.3.2 Indirect-to-Direct Bandgap Transition

In the natural state, TMD materials in their bulk and multilayer forms are indirect bandgap materials. Interestingly, as the sample thickness decreases gradually from a bulk system to one that is monolayer, not only does its bandgap increase in magnitude, but it also evolves into a direct bandgap semiconductor [38, 47, 51, 53, 54, 62, 63].

In the cases of TMD systems with constituent atoms from Group VI transition metals (Mo and W) and chalcogens such as S and Se, they are usually thermodynamically stable in the semiconducting 1H-phase [64]. Both monolayer-WSe_2 [65] and MoS_2 [38, 51] were first computationally predicted to possess such direct bandgap electronic structures at the K/K'-points of their hexagonal Brillouin zone. Figure 1.9 displays the calculated band structure of MoS_2 as it reduces from a bulk and eventually into the monolayer structure where it shows the gradual transition

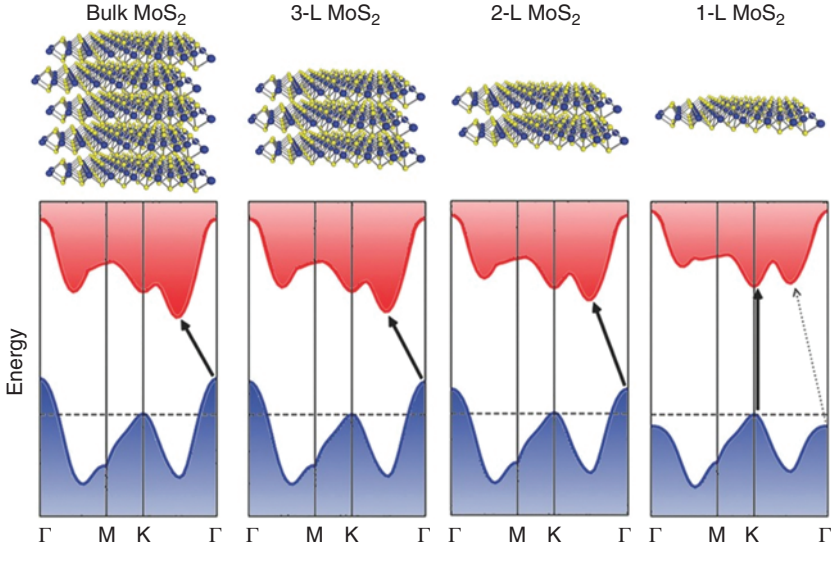

Figure 1.9 Thickness-dependent bandgap properties of semiconducting phase MoS_2 in its bulk, trilayer, bilayer, and monolayer form. With the arrows indicating the lowest energy transitions from the valence to the conduction band, one can see a gradual transition from an indirect (1.29 eV) to a direct bandgap (1.8 eV) with decreasing layer number. This accounts for the significant increase in photoluminescence efficiency of monolayer-MoS_2. Source: Reproduced with permission © 2016 WILEY-VCH Verlag GmbH & Co. KGaA, Weinheim Bonaccorso et al. [66].

from an indirect to a direct electronic bandgap [53, 54]. Besides, the computationally derived electronic bandgap for semiconducting phase MoS_2 shows an increase in magnitude from 0.88 eV in its bulk form to 1.71 eV for monolayer-MoS_2 [67]. The experimentally measured optical bandgap using photoluminescence measurements for monolayer-MoS_2 has been registered to be 2.16 eV where there is a distinct increase in the luminescence efficiency in the monolayer as compared to its bulk and multi-layer forms [53, 54]. Nevertheless, the disparity between the experimentally measured and theoretical value in the monolayer direct bandgap can be attributed to the presence of actual charge interactions in the real monolayer system.

The gradual transition of TMD systems from an indirect bandgap material in its multi-layer form to a direct bandgap system in its monolayer form can be attributed to the presence of interlayer hopping in their multilayer form. Figure 1.10 compares

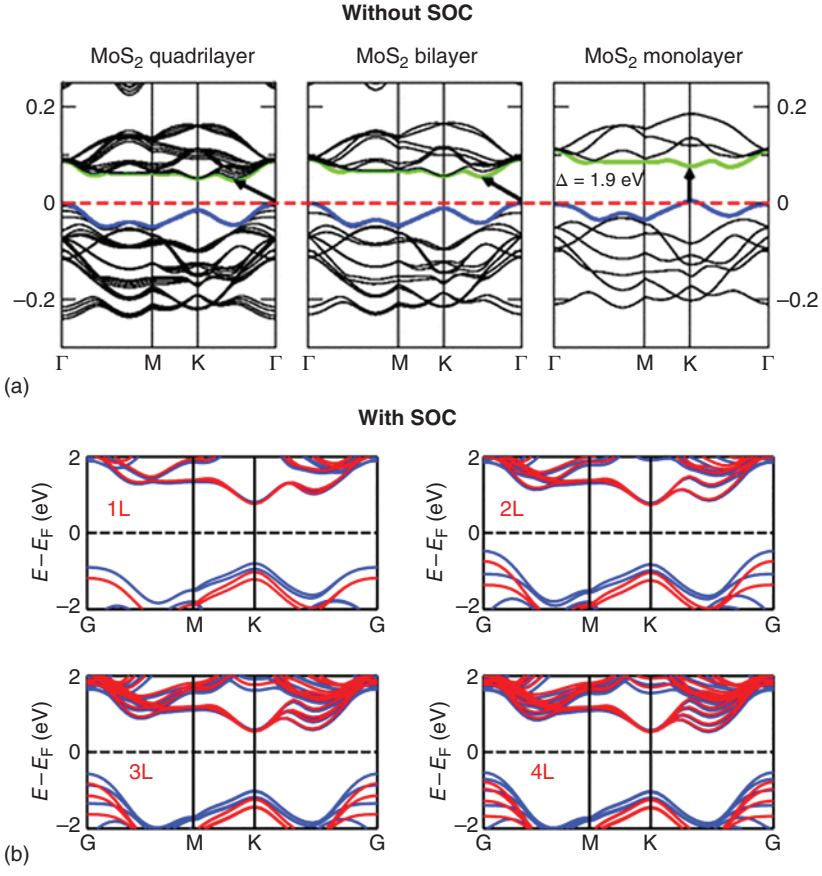

Figure 1.10 Band structures of (a) quadrilayer, bilayer and monolayer MoS_2 without the SOC effects, and (b) that with SOC in consideration. Source: (a) Reproduced with permission from Kuc et al. [62]. Copyright (2011) by the American Physical Society. (b) Reproduced with permission from Wickramaratne et al. [68]. AIP Publishing.

the band structures of WS_2 of different layer numbers with and without the effects of spin-orbit coupling (spin-orbit coupling effects to be discussed in the next section), the band edges at the respective high symmetry points K_v, Γ_v and Q_c (where subscripts C: conduction band; V: valence band) are shown to split with increasing layer number – these are direct evidence of interlayer hopping and the important role that Van der Waals interaction plays in such multilayer systems in dictating the system's electronic structures. The quantity of band splitting at each symmetry point also corresponds to the interlayer hopping strength. One should also note that contributions by the respective transition metal d- or chalcogen p-orbitals also vary at different regions of the electronic band structure. They result in different splitting magnitudes at different points in momentum space.

Notably, the Γ_v and Q_c-points display considerably more pronounced band splitting than K_v. This is because orbital contributions at the K_v-point are attributed mainly to the metal d-orbitals. Conversely, the chalcogen p_z-orbitals dominate the Γ_v and Q_c-points (c.f., Figure 1.7). With this in consideration, it is noted that interlayer charge hopping between the chalcogen p_z-orbitals plays a more significant role in comparison with other orbital interactions. Conversely, such interlayer hopping processes at the K_v-point is comparatively much weaker due to the large spatial separation between the transition metal planes. With increasing layer number, the energy level of the Γ_v-point registers a significant increase while that of Q_c is reduced. Meanwhile, the positions of both the K_C and K_v-points remain largely unchanged in the Brillouin zone. These relative evolution of the energy bands with contributions from both the metal and chalcogen orbitals results in the transformation of band structure from one that comprises an indirect band gap in the multilayer form to a direct bandgap system in the monolayer form.

1.3.3 Spin-Orbit Coupling and Its Effects and Optical Selection Rules

Readers who would like a very comprehensive treatment on this subject can also refer to the review [69]. Without the effects of interlayer van der Waals interaction, the effects of spin-orbit coupling (SOC) will become very prominent on the electronic properties of 2D-TMDs as compared to single-layer graphene. This is attributed to the heavy elemental components in the TMD systems where the SOC strength is directly proportional to the fourth power of the atomic number, Z [70]. Specifically, effects of the transition metal component outweighs that of the chalcogen atoms, particularly with the d-orbitals of the former [70]. For instance, there is a ~0.4 eV band splitting at the K-point in the valence band for W-based (WSe_2 displayed in Figure 1.11a,b) and ~0.2 eV for Mo-based 2D-TMDs (MoS_2 displayed in Figure 1.11c,d) as a result of SOC effects [50, 71–75]. This spin-split ultimately gives rise to the two valence sub-bands which in turn result in the appearance of the notable excitons A and B due to the band transitions at the K/K'-point.

Likewise, a significantly smaller spin-orbit split is also present at the CBM due contributions from the p- and d-orbitals [52, 76–78]. The polarity of the conduction band spin split may also differ depending on the transition metal atomic component. This leads to the lifting of the spin degeneracy of both the conduction and valence

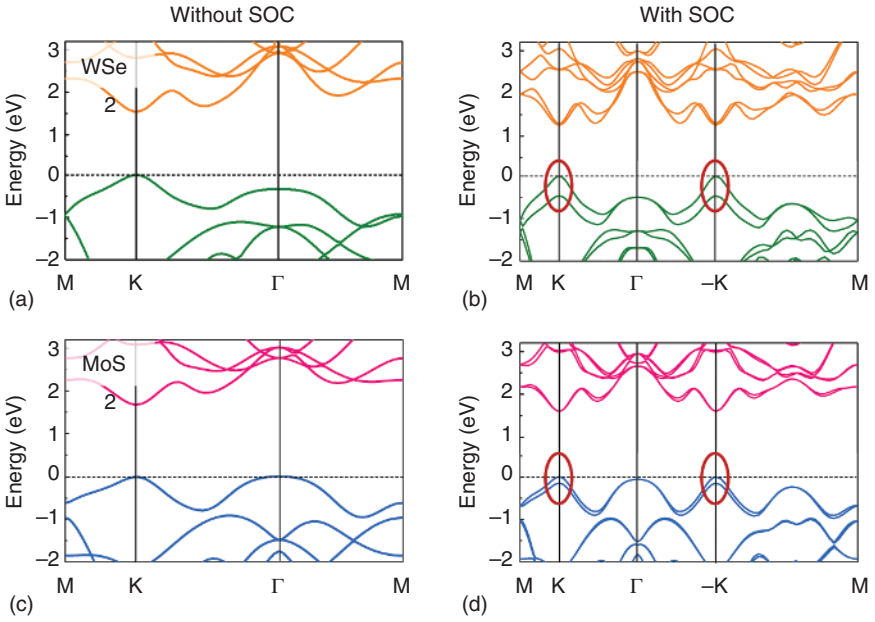

Figure 1.11 Band structure calculations of WSe_2 and MoS_2 monolayers with and without the effects of spin–orbit coupling. (a) Electronic band structure of monolayer-WSe_2 without, and (b) with the effects of spin–orbit coupling. (c) Electronic band structure of monolayer-MoS_2 without, and (d) with the effects of spin–orbit coupling. The valence band splits at the *K*(-*K*)-points are indicated by the red circles. Source: Tang et al. [71]/Reproduced with permission from American Chemical Society.

bands at the K/K'-point. Moreover, spin-splitting at the conduction band results in an energy separation between the spin-allowed and optically active (bright) transitions and the spin-forbidden and optically inactive transitions (dark).

Contributions from the electron-hole Coulomb exchange energy also affect the amplitude of the excitonic state splittings [79–81]. In the case of Mo-based 2D-TMDs, the lowest-energy transition will be the bright exciton [76, 77] as experimentally confirmed [82, 83]. Conversely, dark excitons in W-based 2D-TMDs are located at lower energy positions than their bright counterparts [82, 84–86].

With the spin-splitting effects, chiral optical selection rules apply for interband transitions at the K/K'-points. While the orbital Bloch functions at the conduction band transform with the angular momentum components of ± 1, those at the valence band remain invariant. This renders the optical selection rules for the interband transitions at the K/K' valley to be chiral. In other words, circularly polarized light of orientation $\sigma^{\pm}$ can only couple with interband transitions at the $K^{\pm}$ band, respectively [73, 87–90]. This unique optical selection behavior of 2D-TMDs makes them ideal for the investigation of valleytronic properties and applications [91–93].

While it is possible for the electrons to switch their valley, a spin-flip or a very energetically unfavorable transition is required. Hence, optically-generated electron-hole pairs are generally spin-valley polarized (locked). Hence, by

conducting a spin-polarized excitation, exciton emission of 2D-TMDs can be co-polarized with the laser if the valley polarization lifetime is of similar order or longer than the exciton recombination time.

1.4 Excitons (Coulomb-Bound Electron-Hole Pairs)

An exciton is a quasiparticle bound state formed by an excited electron and hole due to their Coulomb interaction [94]. With the onset of photoexcitation, an electron will be excited from the filled valence band into the empty conduction band, and it will leave a hole in the valence band. With the electron and the hole possessing opposite polarity, they can attract each other via Coulomb interaction and such a many-body system involving a negatively charged conduction electron and a positively charged hole in the valence band can now be simplified. The formation of a bound state form between the electron-hole pair corresponds to a neutral *Exciton* which possesses a strongly-correlated relative spatial displacement between the constituents.

Based on the exciton radius and the Coulomb interactions within the electron-hole pair, two main classes of excitons can arise as a result of *long-range* and *short-range* coupling. With the large dielectric function within the crystal lattice, electric field screening reduces the Coulomb interaction between the electron-hole pairs. Hence, the exciton radii are significantly larger (long-range) in the scale of interparticle distances than the interatomic bond lengths. These are generally known as the *Wannier-Mott* or *large-radius-type* excitons commonly found in semiconducting systems such as GaAs [95] and Cu_2O [96]. With the smaller masses and screened Coulomb interaction, the binding energies of Wannier excitons are generally in the order of ∼0.01 eV [97, 98].

Conversely, the short-range counterpart arises due to the overlapping wave functions of the constituent electron-hole pair at the scales in the order of the crystal lattice constant (e.g. $a_0 \sim 3$ Å for 2D-TMDs) and typically within the range of up to a few unit cells. This class of excitons correspond to the charge-transfer between nearest lattice sites. Besides, typically found in ionic crystals and organic molecular crystals, such electron-hole bound states are known as *Frenkel* Excitons which have binding energies in the order of ∼0.1—1 eV [99–102].

Another important consideration regarding exciton formation due to Coulomb interaction is the self-energy of the electron-hole quasiparticle. This concept of self-energy is related to the repulsion between identical charges which results in an overall increase in the exciton bandgap of the system. It is the energy required to break the interaction between the electron-hole pair in the continuum similar to that of the Rydberg series of the hydrogen atom to create a free particle. Therefore, it is considered an excitonic Rydberg series (excited state of the electron-hole pairs) where the excitonic properties can be experimentally derived with the schematic of the optical absorption in the ideal 2D semiconductor displayed in Figure 1.12.

The presence of many-body interactions in the form of Coulomb interactions leads to the formation of the exciton resonances below the bandgap. Known as the *optical bandgap*, this energy gap is taken with reference to the lowest-energy excitonic

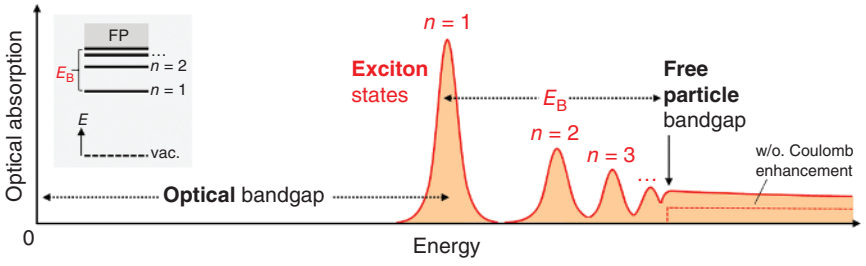

Figure 1.12 Schematic of the optical absorption of an ideal 2D semiconductor. It comprises a series of bright exciton transitions below the renormalized quasiparticle bandgap. Strong Coulomb interaction also enhances the continuum absorption in the energy range beyond the exciton binding energy, E_B. The inset shows the hydrogen atom-like energy level scheme of the exciton states, designated by the principal quantum number n, with E_B of the exciton ground state ($n = 1$) below the free-particle (FP) bandgap. Source: Wang et al. [69]/Reproduced with permission from American Physical Society.

feature in absorption at the exciton ground state ($n = 1$). As seen in Figure 1.12, the optical bandgap is distinct from the so-called *free-particle* band gap – corresponding to the continuum of free electrons and holes (where $n = \infty$). As a result of varying dielectric environments of different 2D systems, it plays a crucial role in tuning both the exciton binding energy and the free-particle bandgap of the system. Interestingly, this results in different systems possessing relatively similar optical bandgaps [103–105].

1.4.1 Exciton Binding Energy

Apart from the dielectric properties of the material in consideration, another key factor dictating the exciton binding energy would be the material's dimensionality. The exciton binding energy can thus be expressed based on the equation [106]:

$$E_n = -\frac{E_0}{\left(n + \frac{\alpha-3}{2}\right)^2} \tag{1.1}$$

where α denotes the material dimensionality, n the principal quantum number, and E_0 is the Rydberg constant.

As a result of this relation, the excitonic properties of 2D systems differ significantly from their 3D counterparts even of the same material. Strong electron-hole interaction results in a significantly different optical spectrum as compared to the 3D counterpart with the formation of a series of new excitonic levels below the quasiparticle bandgap as seen in Figure 1.12. A distinct feature of excitons in 2D systems is that they are strongly confined within the in-plane system where the electronic excitations are restricted within the 2D structure. Unlike excitons found in typical bulk three-dimensional systems, the large spatial overlap between the electron-hole orbitals can be attributed to the effects of quantum confinement. In addition, the electric field between the electron-hole pair can penetrate the

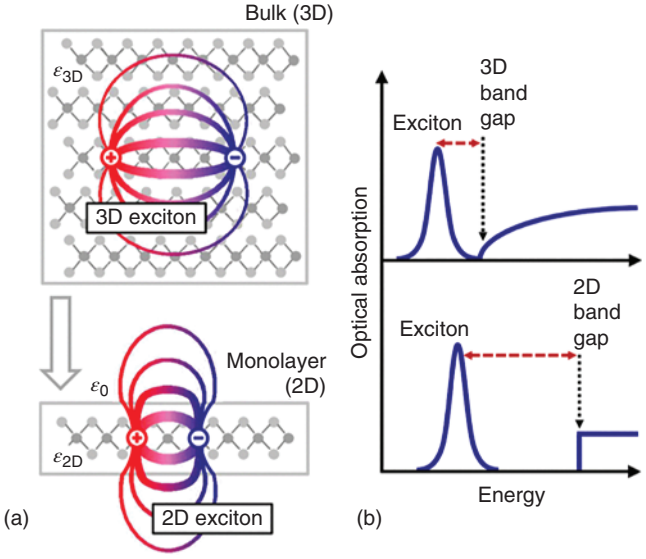

Figure 1.13 (a) Real-space representation of excitons in three-dimensional and two-dimensional systems. The changes in the dielectric environment are schematically represented by the respective dielectric constants ε_{3D} and ε_{2D} and the permittivity of free space ε_0. (b) The effects of dimensionality on the electronic and excitonic properties schematically represented by the optical absorption spectra. Change in dimensionality from 3D to 2D leads to an increase in the band gap and exciton binding energy represented by red dashed line. Source: Reproduced with permission Chernikov et al. [107]/Reproduced with permission from American Physical Society.

2D-plane where charge screening is absent. These features unique to 2D systems lead to the significant enhancement in the Coulomb attraction which in turn results in a larger excitonic binding energy as compared to the 3D counterpart (Figure 1.13a). For instance, while excitons in bulk WS_2 have binding energy of $\sim$ 50 meV, excitons in monolayer-WS_2 have binding energies of $\sim$ 320 meV [107].

As a result of the dimensionality, 2D excitons have unique properties with a combination of both Wannier-Mott and Frenkel features – they have both large Bohr radii and are strongly bound, respectively. In general, the exciton Bohr radii are in the order of ~1 nm [108–110]. Based on quasiparticle GW band structure calculations, the effective Bohr radius for MoS_2 is 9.3 and 13.0 Å in its monolayer and bilayer form, respectively, at the low-dimension limit [72]. While these may not appear to a significant magnitude, they are sufficiently large relative to the in-plane lattice constant of 2D-TMDs in general (~3 Å). Hence, the Wannier-Mott exciton theory is still applicable in such 2D systems. Correspondingly, the effective exciton binding energies stood at 0.224 and 0.106 eV in its monolayer and bilayer form, respectively. Interestingly, an alternative study has even reported an exciton spread over 65 Å [111]. Further unique excitonic effects attributed to the two-dimensional features come in the form of a step-function for gapped systems with dipole-allowed interband transitions (Figure 1.13b) [107].

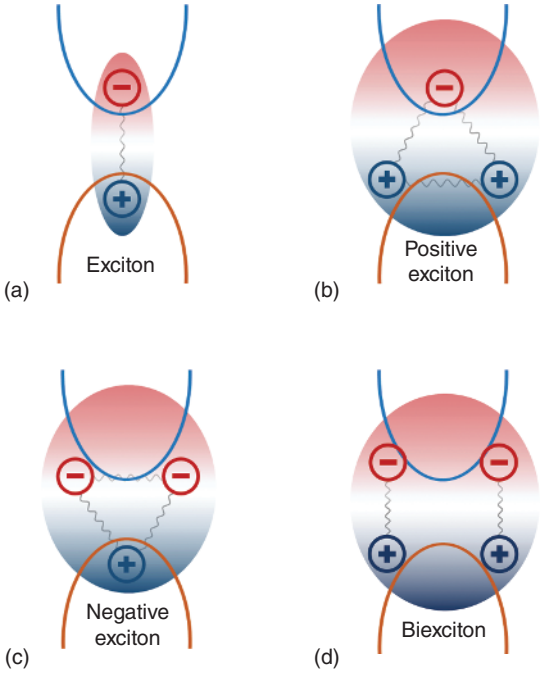

Figure 1.14 Schematic representation of quasiparticles. (a) Neutral exciton, (b) positive trion, (c) negative trion, and (d) neutral biexciton.

1.4.2 Excitons and Other Complex Quasiparticles

With increasing exciton (Figure 1.14a) and other charged-particle concentrations, complexes including the three-particle charged excitons known *trions* (Figure 1.14b,c) [71, 112, 113], and four-particle *bi-excitons* (Figure 1.14d) can also be formed [114, 115]. In the case of bi-excitons, their binding energies (~52 meV for monolayer-WSe_2) is more than an order of magnitude greater than those in conventional quantum-well systems [116]. This is attributed to the effects of both strong carrier confinement and reduced and non-local dielectric screening [108, 117].

While excitons and biexcitons are of neutral polarity due to their two-particle or four-particle composition, charged excitons known as a *trion* have odd-numbered (3) particles. Depending on its polarity, it can either comprise two holes and an electron (positive trion – Figure 1.14b) or two electrons and a hole (negative trion – Figure 1.14c) [112]. These charged quasiparticles are only formed in systems where excess charges are present and implies that the trion emission intensity serves to quantify the excess charge concentration.

While excitons in 2D-TMDs have binding energies in the order of ~102 meV, the binding energy of trions are usually an order of magnitude smaller but are still considerably larger than excitons in conventional semiconducting systems [116]. In many cases, both the exciton and trion peaks can be observed in photoluminescence experiments particularly at low temperatures. There are also instances where trions are observed in gated samples at an additional line 20–35 meV below the main

exciton emission line and these can be attributed to the emission from charged excitons of both polarity [112, 118].

While exciton energy can vary as a result of varying Fermi energy induced by electronic gating process, the trion energy usually remained largely unchanged [112]. Besides, the energy split between the exciton and trion energy is expected to be linearly-dependent on the Fermi energy [119]. Hence, the trion binding energy can be estimated via the differences between the respective trion position and the associated exciton peak position based on the following expression [71, 112]:

$$E_X - E_{X'} = E_{\text{bin}} + E_F \tag{1.2}$$

where E_X and $E_{X'}$ denote the peak positions of the exciton and the associated trion, respectively; E_{bin} represents the trion binding energy while E_F is the shift in Fermi level relative to the conduction band maximum at the K/K'-point in the Brillouin zone [112]. In typical experimental studies, to obtain a reasonably good estimate of the trion binding energy, E_{bin}, is estimated for data sets at low temperature where E_{F} in Eq. (1.2) can be assumed to be negligible (i.e. $E_F \approx 0$) [71]. A series of analyses conducted show that the trion binding energy is in the range of ~18 meV [112] and some show marginally higher magnitudes at ~40 meV [71, 113] in systems such as MoS_2 and WSe_2 monolayers. The considerable magnitude of the trion binding energy suggests the importance of trion activities in 2D-TMD systems even at elevated temperatures of the order $\sim 10^2$ K.

1.4.3 Resonant Excitons in 2D-TMDs

While the aforementioned excitons typically occur within the direct bandgap of the relevant semiconducting materials and 2D systems, the presence of strong many-body interactions can also lead to the formation of unique high-energy regime quasiparticles known as high-energy *resonant excitons* – excitons that occur at energy levels well above the bandgap especially in the UV-Vis regime where higher energy bands are involved in their formation [120, 121]. In 2D systems, these unique resonant excitons are theoretically predicted [122] and have already been experimentally observed in monolayer-graphene [123]. Besides, such excitons have also been observed in 2D-TMDs including monolayer-WSe_2 [71]. The presence of resonant excitons in monolayer-WSe_2 and its absence from 2D-TMDs such as monolayer-MoS_2 where the atomic number of the constituent elemental components suggests the significant influence that SOC plays in the formation of this high-energy quasiparticle. This is attributed to the heavier atomic constituents of WSe_2 [70], where the SOC strength is directly proportional to the fourth power of the atomic number, Z. Therefore, it is specifically the transition metal atomic mass that plays a more significant role than the chalcogen atoms [70].

Specifically in the case of monolayer-WSe_2 as compared to systems such as monolayer-MoS_2, even though they share similar crystal structure in the semiconducting 1H-phase (Figure 1.15a), the strong SOC effects considerably transform the electronic and optical structures of monolayer-WSe_2. By combining this with the effects of strong electronic correlations, SOC facilitates the formation of

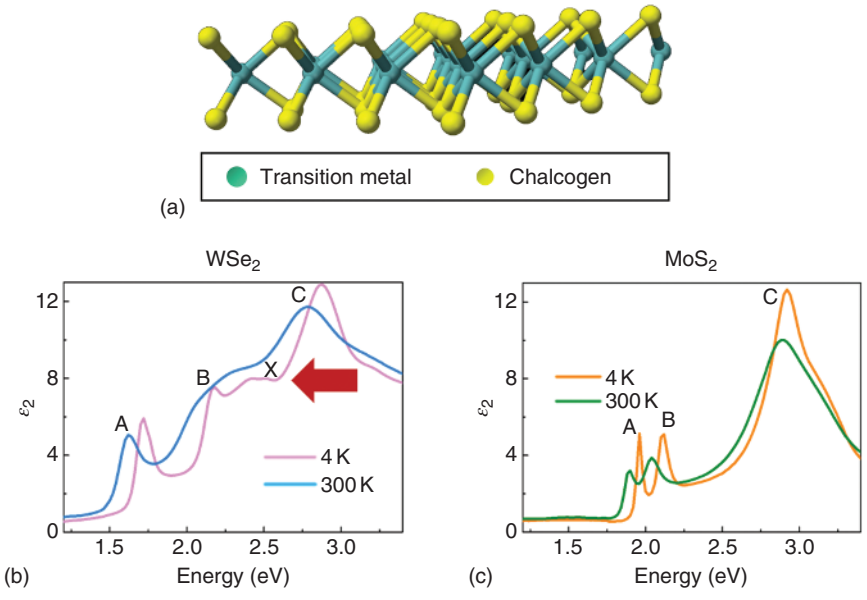

Figure 1.15 (a) The typical lattice structure of 1H-phase 2D-TMDs. Despite sharing similar lattice structures, the optical properties of different 2D-TMD species are significantly different. Source: Adapted from Tang et al. [71]. Examples shown here include the ε_2 spectra of (b) WSe_2 and, (c) MoS_2 monolayers. Source: Tang et al. [71]/Reproduced with permission from American Chemical Society.

three-dimensional resonant excitons in the high-energy visible regime (~2.4 eV) that can be directly observed via the optical response spectra (denoted by arrow in Figure 1.15b – c.f., Figure 1.20d). In contrast, this optical artifact is absent from monolayer-MoS_2 (Figure 1.15c – c.f., Figure 1.20a). As such, the fundamental understanding of high-energy resonant exciton is crucial in unraveling the intricate electronic structures of 2D materials in general, thus facilitating novel optoelectronic applications especially in the UV-Vis regime [71, 124–127].

1.5 Experimental Studies and Characterization of 2D-TMDs

Given the diverse range of potential applications that 2D-TMDs have promised, extensive characterization studies have been performed to uncover their intrinsic properties. This ranges from their optical bandgap to the electronic structures in the respective structural phases. With the unique low-temperature properties that several 2D-TMD systems possess, their morphologies have also been extensively reported especially in relation to their charge density wave structures. This section will delve slightly deeper into the respective techniques employed to uncover the unique properties of 2D-TMD systems. A brief overview of the synthesis techniques will also be provided.

1.5.1 Synthesis of 2D-TMDs

While MoS_2 and WS_2 are the main naturally-occurring TMD materials in the form layered crystals, single crystalline TMDs are good sources of monolayer TMDs for experimental characterizations and device fabrications [3, 64, 128]. Hence, 2D-TMDs are derived from bulk natural or synthetic crystals using mechanical exfoliation similar to how graphene is derived from graphite single crystals. While this is a convenient technique to obtain low-dimensional TMD samples for rapid experimental characterization and development of micro-device prototypes, the mono- or bilayer materials are generally non-scalable due to the random feature of the exfoliation technique and that the samples obtained are generally in the $\sim 100\,\mu m^2$ scale at the most.

An alternative to the mechanical exfoliation process would be the use of liquid-phase exfoliation with organic solvents [129, 130] and the Li-intercalation [42, 131] techniques. They allow for the synthesis of solutions containing TMD flakes at controllable thicknesses. Nevertheless, it may be difficult to regulate the phases of the synthesized 2D-TMDs particularly via the Li-intercalation technique for different species due to their relative stability. A mixture of different phases may be found over a large area of the 2D-TMDs due to the phase transition processes taking place within the sample [131–133] and the random stacking of the flakes in certain regions that results in inconsistency of the in-plane resistance may hinder the utilization of the films [131].

1.5.1.1 Chemical Vapour Deposition

Chemical vapour deposition (CVD) is a very efficient and cost-effective technique in the synthesis of high-quality and large-area 2D-TMDs (see schematic in Figure 1.16a). A very comprehensive treatment on this synthesis technique

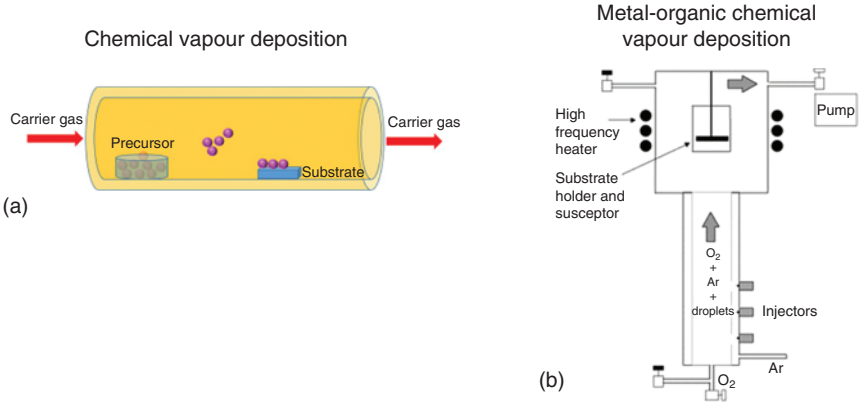

Figure 1.16 Schematics of CVD and MOCVD synthesis methods of TMD thin-films. (a) CVD is based on the direct chemical reaction between the precursor materials. (b) MOCVD works on the decomposition of metal–organic precursors and thereafter, their chemical reaction. Source: (a) Reproduced from Mittal et al. [134]/with permission of ELSEVIER. (b) Reproduced from Niu et al. [135]/with permission of ELSEVIER.

has been presented in Ref. [136] . For samples such as WSe_2 and MoS_2, WO_3 (MoO_3) and Se (S) powders react at elevated temperatures that lead to the eventual growth of the TMD monolayers on substrates such as SiO_2 and sapphire (Al_2O_3) [60, 137–139]. While CVD-grown 2D-TMDs on SiO_2 have greater instances of random lattice orientation which in turn would result in the formation of different grain boundaries [139, 140], those synthesized on Al_2O_3 have better control of domain orientations, thereby promoting their epitaxial growth [141]. The effective control and epitaxial growth of 2D-TMDs are crucial factors for the better control of the electrical and optical properties of large-area films.

Metal–organic CVD (MOCVD) is a further extension to the CVD technique based on their gas-phase precursors [142–145] where they are supplied to the main chamber with controlled flux (Figure 1.16b). Beside producing 2D-TMD samples with good electron mobility such as monolayer-MoS_2 of $\sim 30\,cm^2\ V^{-1}\ s^{-1}$[143], a diverse variety of 2D-TMDs including $MoSe_2$ [146, 147], WS_2 [145, 148–152], WSe_2 [144, 153–155], ReS_2 [156–158], $ReSe_2$ [159], $MoTe_2$ [160, 161] and WTe_2 [161] have been grown.

1.5.1.2 Molecular Beam Epitaxy

Another notable method to synthesize high-quality monolayer TMDs at a scalable level would be the Molecular Beam Epitaxy (MBE) [162]. Figure 1.17 presents the schematic of this synthesis technique. In this case, several atomic sources are present in an ultra-high vacuum chamber ($\sim 10^{-10}$ mbar) to create the molecular

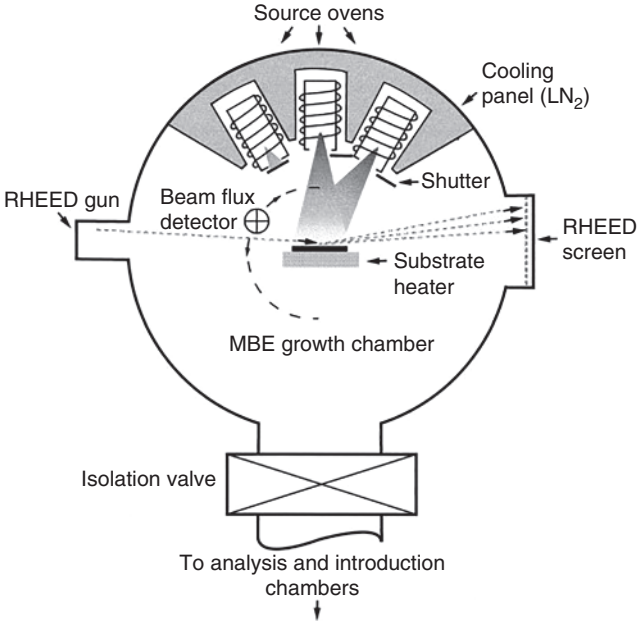

Figure 1.17 MBE involves high-purity elemental source materials that are co-evaporated in ultrahigh vacuum conditions. Source: Reproduced with permission Arthur [163].

beams. Molecular deposition is then conducted on a preheated substrate such as gold, Highly Ordered Pyrolytic Graphite (HOPG) while growth parameters including the film thickness and substrate crystallinity are monitored *in-situ* by reflection high-energy electron diffraction (RHEED) and low-energy electron diffraction.

With the availability of different substrates as mentioned earlier, 2D-TMDs can be synthesized on other layered materials and passivated surfaces without concern about lattice matching conditions due to their lack of dangling bonds. Besides, the van der Waals forces of interaction can be exploited for the epitaxial growth process where the substrate lattice structure is utilized to manipulate the monolayer crystal orientation [141]. Samples that are MBE-synthesized are generally of high-quality and crystallinity. Hence, they are generally characterized *in-situ* using high-precision systems such as angle-resolved photoelectron spectroscopy and scanning tunneling microscopy for fundamental studies and investigations [164, 165]. The effectiveness of this technique also allows for the synthesis of highly-ordered and crystalline vertical heterostructures such as $MoSe_2$/graphite [166], $SnSe_2/WSe_2$ [167] and $MoSe_2/Bi_2Se_3$ [168]. These exceptional features render MBE a highly versatile technique to synthesize 2D-TMDs and their heterostructures to study them at the fundamental level.

1.5.2 Optical Characterization

A diverse array of optical techniques is available to determine the optical properties of 2D-TMDs. Techniques such as photoluminescence and absorption edge spectroscopy serve as ideal methods to characterize optical band gaps [169]. Meanwhile, the absorption spectra of 2D-TMDs contain more information pertaining to their optoelectronic properties depending on their spectral regions. For instance, while the low-energy regions are generally dominated by the excitonic features, the high-energy regime contains information pertaining to interband transition states and band-nesting features related to the contours of the electronic band structures.

1.5.2.1 Photoluminescence

It has first been demonstrated that monolayer-MoS_2 possesses a direct bandgap and that results in a strong photoluminescence (PL) [53, 54]. Besides, PL can be utilized to demonstrate the indirect-to-direct bandgap transition of TMD materials when they are gradually reduced from a multi-layer to a monolayer crystal. While techniques such as the scanning tunnelling spectroscopy the material's free-particle bandgap, E_0, PL characterizes the exciton transition energy, E_X. Of course, there are different types of excitons attributed to different forms of interband transitions in both atomically thin nanomaterials and heterostructures based on the schematic in Figure 1.18a [170]. By combining these two sets of measurements, one can arrive at the exciton binding energy which has been determined to be ~0.55 eV for monolayer-$MoSe_2$ [164] and ~0.37 eV for monolayer WSe_2 [172].

As mentioned in the earlier sections, spin-orbit coupling has a significant impact on the optical dichroic properties of 2D-TMDs in the form spin- and valley-selective excitonic states. Hence, PL excitation in the form of circularly polarized light can

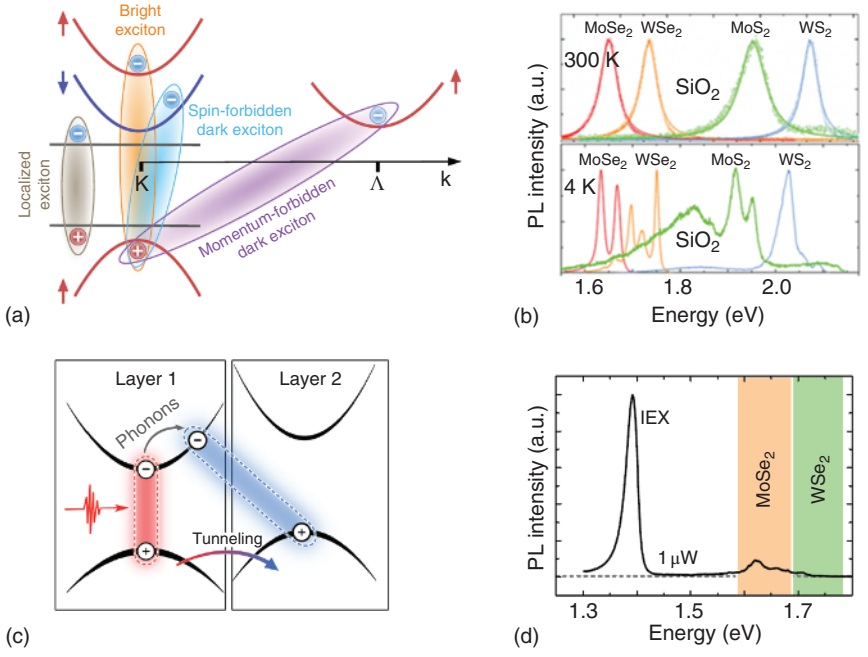

Figure 1.18 Different excitons in low-dimensional layers and heterostructures. (a) Schematic showing different types of excitons and how they take place attributed to different transitions. (b) (a) Comparing the PL spectra of the respective 2D-TMDs MLs at $T = 300$ K and $T = 4$ K when deposited directly onto SiO_2 and when capped with hBN. The appearances of additional PL peaks at low temperature indicate the presence of localized excitons due to lattice defect especially for the samples deposited directly on SiO_2. (c) Schematic showing how interlayer excitons appear where the electrons-holes are located in different constituent layers. (d) PL spectrum of a $MoSe_2/WSe_2$ heterostructure which shows the strongly PL response of interlayer excitons. Source: (a) and (c) Mueller and Malic [170]/Springer Nature/Licensed under CC BY 4.0. (b) [104]/American Physical Society/Licensed under CC BY 4.0. (d) Nagler et al. [171]/Reproduced with permission from IOP Publishing.

selectively induce excitonic transitions in either the K or K'-valley. Besides theoretical predictions [73], this unique effect has been well-verified experimentally [88–90, 173–178].

With the inevitable onset of surface impurities, defects, and lattice strain in 2D-TMD materials, PL serves as an effective technique to analyze electron-hole pairs (i.e. localized excitons – Figure 1.18a) that are bound in such defect-induced potential wells. During low-temperature PL measurements, apart from the usual bright exciton emission, a few other narrow optical resonances can also be observed (Figure 1.18b) and these are attributed to excitons trapped in local potential wells [104]. Nevertheless, such features are not visible at high temperature because the localized excitons are easily displaced by thermal excitations. These localized exciton states can be commonly found in monolayer TMDs [179–183] and crystal edges [179] where defects and discontinuities are commonly found.

The presence of Van der Waals interactions between stacked 2D-TMD layers [184] also yield interesting phenomena such as the formation of interlayer excitons where the components of the electron-hole pairs are situated in different TMD layers (Figure 1.18c) [171, 185–191]. The presence of interlayer excitons has been confirmed by multiple PL studies [171, 185, 186, 188]. Optical responses of interlayer excitons tend to be more prominent than their intralayer counterparts under weak excitation. In this study involving the time-resolved PL of time-resolved PL of the $MoSe_2/WSe_2$ heterostructure (Figure 1.18d), the long-lived excitonic response appears at the energy below the intralayer excitons. This can be attributed to the highly-efficient interlayer charge-tunneling processes that separate electron-hole pairs generated by optical absorption in the respective monolayers [171].

1.5.2.2 Spectroscopic Ellipsometry

Spectroscopic ellipsometry is a non-destructive and precise optical characterization technique that measures the thickness, optical properties, and surface morphology of samples. This is done by elucidating the complex reflection using optical modeling methods. Unlike other experimental techniques such as transmission and reflectivity measurements, both the real and imaginary components of the optical parameters can be derived simultaneously without the need for Kramers-Kronig transformations – an analytical technique that connects both the real and imaginary components of the complex optical function.

Having this as another major advantage, the collective features of spectroscopic ellipsometry make it a powerful and ideal system over a wide range of applications in both industrial and research disciplines.

Spectroscopic ellipsometry measures the change of light polarization upon its reflection from the sample. A schematic of the experimental setup is displayed in Figure 1.19a. The detector of spectroscopic ellipsometry measures the quantities, Ψ and Δ at each corresponding wavelength/photon energy. Parameter Ψ denotes the ratio between the amplitude of *p*- and *s*-polarized reflected light while Δ their phase difference. Specifically, *p*-polarized light has the electric field vector parallel to the plane of incidence while s-polarized light consists of electric field vector perpendicular to the incident plane (Figure 1.19b,c).

Typically, the energy range that is commonly used for spectroscopic ellipsometry measurement is the ultraviolet–visible (UV-Vis) regime (~0.5–6 eV). In this range, sample properties such as the optical band structures and bandgaps can be investigated. Nevertheless, other regions of the electromagnetic spectrum have also been used in spectroscopic ellipsometry measurements.

Spectroscopic ellipsometry serves as an effective technique in the characterization of 2D-TMDs. In this example, temperature-dependent high-resolution Spectroscopic Ellipsometry is conducted at temperatures between 4 and 300 K to systematically investigate the optical and excitonic properties of both 1H-phase WSe_2 and MoS_2 monolayers. Figure 1.20a,b display the real, ε_1, and imaginary, ε_2, components of dielectric function of monolayer-MoS_2 at 4 and 300 K. Meanwhile, the respective ε_1 and ε_2 spectra of monolayer-WSe_2 are displayed in Figure 1.20c,d. The optical parameters, ε_1 and ε_2 functions, of both the WSe_2 and MoS_2 monolayers are consistent with

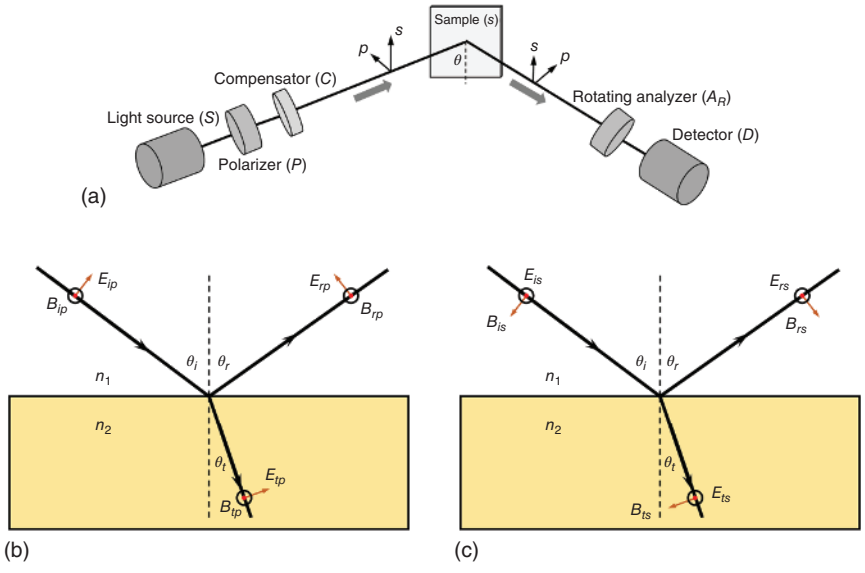

Figure 1.19 (a) Schematic of spectroscopic ellipsometry with the rotating-analyzer configuration. Electric and magnetic field for (b) *p*-polarized and (c) *s*-polarized waves during before and after reflection off the sample surface during the spectroscopic ellipsometry characterization process. Source: (a) Fujiwara [192]/Reproduced with permission from John Wiley & Sons.

other optical characterization reports of the same materials using either ellipsometric or reflectance techniques [53, 193].

Particularly, the ε_2-spectra of both MoS_2 and WSe_2 monolayers indicate that their optical and electronic structures differ significantly. As mentioned earlier, these distinctions are made more prominent in view of the similarities in their 1H-phase lattice structures. The differences in the optical properties must be attributed to other properties beyond the lattice structure for this class of materials. As such, a detailed investigation is needed to unravel the factors affecting the optoelectronic properties of 2D-TMDs.

To analyze the optical structures of both MoS_2 and WSe_2 monolayers, one can observe distinct peaks labeled *A* and *B* in the ε_2 spectrum (~1.96 and ~2.11 eV, respectively at 4 K) of monolayer-MoS_2 (Figure 1.20b – c.f., Figure 1.15c) have been ascribed to the excitonic transitions at the K/K'-points [194]. The strong inter-band transition (broad feature labelled as *C*) is attributed to the transitions in the region around the Γ- and *M*-points of the Brillouin zone where the conduction and valence bands are nested. This band-nesting feature arises due to the presence of van Hove singularities in the electronic band structures of MoS_2 and other 2D-TMDs (see also calculation results previously presented in Figure 1.11b) [195].

The ε_2 spectra of monolayer-WSe_2 also contain the distinctive peaks *A*, *B*, and *C* whether at low or ambient temperature (Figure 1.20d – c.f., Figure 1.15b). However, there is a distinct peak labeled as *X* located between peaks *B* and *C*. This feature is absent from monolayer-MoS_2 (Figure 1.20a). Interestingly, at the

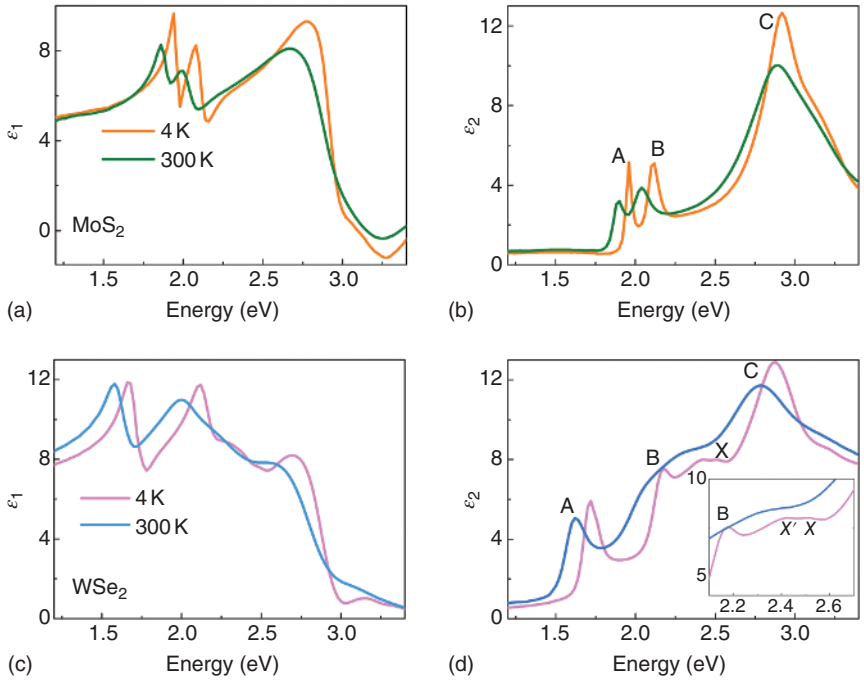

Figure 1.20 (a) ε_1 and (b) ε_2 dielectric functions of monolayer-MoS_2 at 4 and 300 K. (c) ε_1 and (d) ε_2 dielectric functions of monolayer WSe_2 at 4 and 300 K. Inset: Enlarged region of ε_2 indicating the presence of resonant exciton peak *X* and its associated trion *X′* at low temperature. Source: Tang et al. [71]/Reproduced with permission from American Chemical Society.

low-temperature below 100 K, peak *X* splits into two separate peaks – *X* and *X′* (~2.36 and ~2.49 eV, respectively – see inset Figure 1.20d). With reference to the ε_2 spectra of monolayer-MoS_2, peak *A* at ~1.72 eV and *B* at ~2.18 eV of monolayer-WSe_2 can be ascribed to the excitonic transitions at the *K*/*K′*-points in the Brillouin zone of monolayer-WSe_2 [50]. Meanwhile, the strong optical feature *C* at ~2.88 eV, corresponds to band-nesting around the *Γ* and *M*-points in the Brillouin zone of monolayer-WSe_2 [194].

While the origins of peaks *A*, *B* and *C* are well-accounted and explained in both the optical spectra of monolayer-MoS_2 and WSe_2, features *X* and *X′* (located at ~2.36 and ~2.49 eV, respectively) are only present in monolayer-WSe_2. While previous optical studies involving WSe_2 have attributed the appearance of *X* and *X′* to the effects of the Se *p*-orbitals or the intralayer effects that arose due to overlapping Se p- and W d-orbitals [195, 196], the explanation to properly account for the distinct features of *X* and *X′* remains unclear. This is because prior fundamental studies generally involved bulk or multilayer systems where interlayer interactions are considered. By combining temperature-dependent high-resolution spectroscopic ellipsometry down and high-energy Photoluminescence spectroscopy, feature *X* has been identified and attributed as a visible-range 3D resonant exciton in monolayer-WSe_2 [71].

The experimental study is also integrated with an extensive first-principles study to unravel the significant influence that spin-orbit coupling plays in the formation of this resonant exciton through the transformation of the electronic and optical structures of monolayer-WSe_2. With the presence of strong electronic correlations in monolayer-WSe_2, SOC facilitates the formation of three-dimensional resonant excitons in the visible regime that appear as peak *X* as confirmed in the collective analysis of both the spectroscopic ellipsometry and PL spectra.

Having witnessed the effectiveness of spectroscopic ellipsometry to characterize and identify important optical features of 1H-phase 2D-TMDs, it can also be employed to identify important optical structures in other structural phases as discussed in the next study.

A case in point would be the studies to monitor the 1H-1T′ phase transition process of monolayer-MoS_2 and WSe_2 through a high-temperature annealing process. After being transferred onto gold or other metallic substrates, optical characterization is conducted on monolayer-MoS_2 (MoS_2/Au) – see Figure 1.21 – and WSe_2 (WSe_2/Au) – see Figure 1.22 – after annealing at the respective temperatures. As presented in Figure 1.21b, at the optimal annealing temperature of MoS_2/Au, note the appearance of a broad mid-infrared pre-peak at the low-energy region (~0.6–1.5 eV)

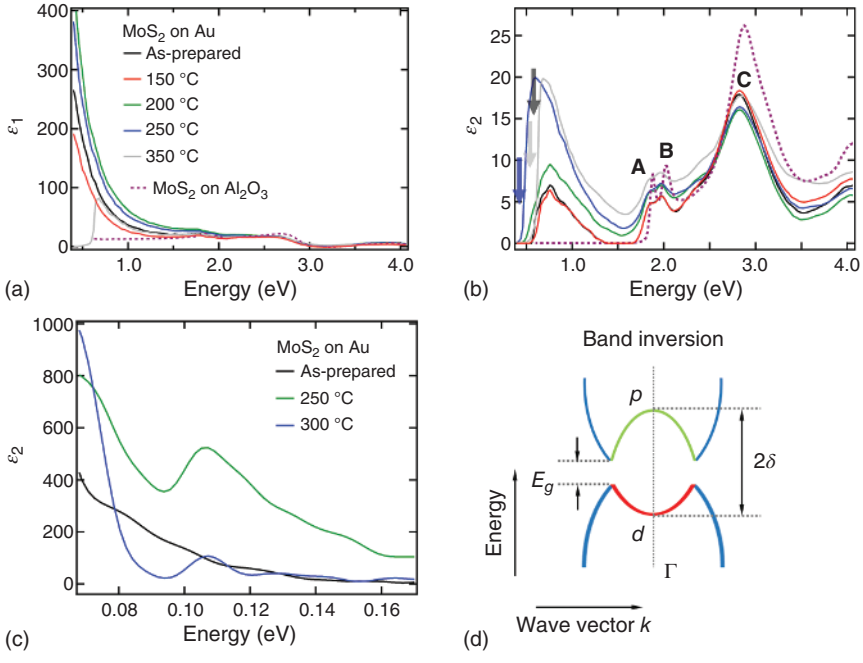

Figure 1.21 Dielectric functions (a) ε_1 and, (b) ε_2 of monolayer MoS_2/Au annealed at the respective temperatures and on Al_2O_3 substrate. (c) ε_2 spectra of monolayer-MoS_2/Au in the far-infrared regime measured using IR-VASE spectroscopic ellipsometry after annealing the sample at the stipulated temperatures. (d) Schematic band structure diagram of 1T′-phase 2D-TMD. Band inversion leads to the presence of the fundamental gap, E_g, and the inverted gap, 2δ. Source: Yin et al. [60]/Springer Nature / Licensed under CC BY 4.0.

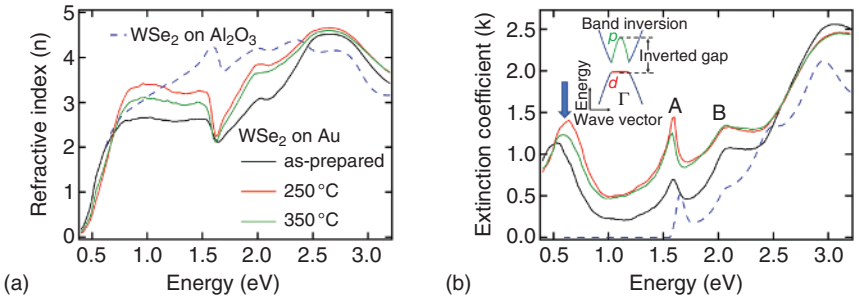

Figure 1.22 (a) Refractive index, $n(\omega)$, and (b) extinction coefficient, $\kappa(\omega)$, of WSe_2/Al_2O_3 and WSe_2/Au annealed at the stipulated temperatures measured by high-resolution spectroscopic ellipsometry. Inset shows the schematic band structure of 1T′-phase monolayer-WSe_2. Similar to monolayer-MoS_2, the lattice distortion together with the strong electron-electron correlations in 1T′-phase WSe_2 induces a band inversion in the vicinity of the Γ-point. This lowers the W *d*-orbital below the Se *p*-orbital and opens an inverted gap, 2δ. Source: Yin et al. [197]/John Wiley & Sons/Licensed under CC BY 4.0.

in the ε_2 spectra. Furthermore, another peak feature is observed in the far-infrared regime which can been attributed to the fundamental gap, E_g, of 1T′-phase MoS_2 at ~0.10 eV upon sample annealing at 250 °C (Figure 1.21c).

The appearances of the mid-infrared and far-infrared features correspond to the inverted gap, 2δ, and fundamental gap, E_g, of 1T′-phase MoS_2 (see schematic of the 1T′-phase band structure in Figure 1.21d). The presence of the pre-peaks along with peaks *A*, *B*, and *C* belonging to 1H-phase MoS_2 can be attributed to the coexistence of the monolayer in both 1H and 1T′-phase.

A similar result is registered for monolayer-WSe_2/Au undergoing the same annealing-induced phase transition process. Unlike the MoS_2/Au sample, the annealing temperature-dependent complex refractive indices ($N(\omega) = n(\omega) + i\kappa(\omega)$) is displayed (Figure 1.22). With the 1H-1T′ phase transition process taking place at higher annealing temperatures, the refractive index, $n(\omega)$, increases significantly in the spectral region between 0.8 and 2.5 eV when the sample is annealed at 250 °C (Figure 1.22a), and then reduces upon further annealing at 350 °C. Similar annealing temperature-dependent trend can be observed in the κ spectra as the ε_2 spectral where the mid-infrared feature attributed to the inverted gap can be observed (Figure 1.22b).

1.5.2.3 Raman Characterization

Similar to PL and Spectroscopic Ellipsometry, Raman spectroscopy is a fast, non-destructive and efficient optical characterization technique that provides structural and electronic information of materials under high spectral and spatial resolution where a comprehensive treatment of its characterization technique can be found in the review [198] and the previous book publication [199]. Based on the fundamental lattice vibrations of TMD materials in the monolayer, multilayer and heterostructure(al) form, one is able to derive essential and detailed information pertaining to properties such as interlayer coupling, spin–orbit splitting and external perturbations.

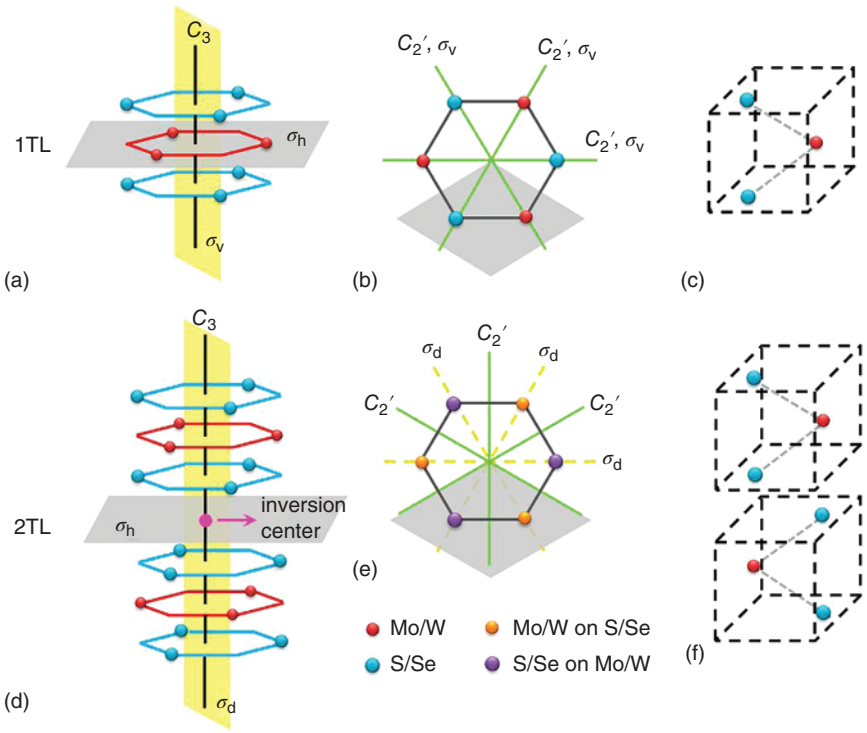

Figure 1.23 Comparing the symmetry operations between a monolayer (1TL) and bilayer (2TL) TMD systems. (a) Side view of a monolayer (odd number) where the axis of the C_3 operations (clockwise and anticlockwise) are denoted by the black vertical line. The horizontal (σ_h) and vertical (σ_v) reflection operations are depicted by the gray and yellow planes, respectively. (b) The monolayer plane view from the top where the axes of the C_2' operations are denoted by the green lines lying in the σ_h plane. The top view of the σ_v planes is also represented by the green lines. The gray diamond displays the unit cell of the crystal view from the top. (c) Side view of the unit cell monolayer, comprising an M and two X atoms. (d) Side view of a bilayer (even number) with the /AbA BaB/ stacking configuration where the C_3 operations axis is denoted by the black line. The inversion centre has been denoted by the pink circle. The horizontal (σ_h) and dihedral (σ_d) reflection operations are represented by the gray and yellow planes, respectively. (e) The bilayer viewed from the top where the purple spheres represent the X-atom above the M-atom and vice versa for the orange spheres. The axes of the three C_2' operations are denoted by the green lines lying in the σ_h plane. The σ_d planes viewed from the top are represented by the yellow dashed lines with the gray diamond demarcating the unit cell. (f) The bilayer unit cell viewed from the side containing four X atoms and two M atoms. The two layers are represented by two dashed boxes. Source: Zhao et al. [201]/Reproduced with permission from American Chemical Society.

Differences in the TMDs structural phases and symmetries in turn result in their distinct electronic structures. Given the unique symmetry of 2D-TMDs in their 1H/3R-phase (D_{3h}) and 1T-phase (D_{3d}), they can be easily distinguished based on Raman analysis [200].

While bulk TMDs have 24 symmetry operations, this number is significantly reduced in the mono- and few-layered systems of 12 in cases of either even or odd

layer numbers. The symmetry operations of odd and even layer numbered systems are illustrated using a mono and bi-layer structure as shown in Figure 23 [201].

Experimentally, Raman scattering was first used to characterize monolayer-MoS_2 [201] where the evolution of the specific Raman modes is shown to vary with layer thickness. Notably, the Raman active vibrations E^1_{2g} and the A_{1g} modes are observed near 400 cm^{-1} at ~384 cm^{-1} and ~415 cm^{-1}, respectively. While the E^1_{2g} is an in-plane vibration mode that corresponds to the opposing vibrations of the in-plane Mo and S atoms, A_{1g} is an out-of-plane mode corresponding to the opposing vibrations of the two out-of-plane S atoms [201–203].

It is observed in Figure 1.24 that with decreasing layer number, the in-plane E^1_{2g}-mode registers a blue shift while the A_{1g}-mode registers an opposite trend with a red shift. These layer-dependent wave number evolutions are consistent with the trend as the MoS_2 transforms from a bulk material to a few-layered system [205]. Meanwhile, the opposite layer-dependent trends between the respective vibration modes suggest the effects of inter-layer interactions and stacking-induced structural changes and the long-range Coulomb interlayer interactions which has an effect even towards the intralayer bonding and lattice dynamics [206].

This similar technique is also utilized to analyze the thicknesses of different TMD species such as $MoSe_2$ [207, 208], WS_2 [209, 210] and WSe_2 [201, 210, 211] where both the E^1_{2g} and A_{1g} vibration modes are examined concurrently and similar thickness-dependent trends have been yielded with the example of WSe_2 in Figure 1.25.

Apart from determining the layer-dependent properties of TMD materials, Raman spectroscopy is also an effective means to distinguish their respective structural phases. Factors such as lattice strain and charge-doping have direct impacts on the phase transition dynamics in 2D-TMDs and Raman spectroscopy can directly analyze the evolving Raman modes as a result of these effects [212].

When considering the 1H-1T′ phase transition of monolayer-MoS_2, it has been demonstrated that upon electron-doping, there is a red-shift in the A_{1g}-mode while the E^1_{2g}-mode remains unchanged [213]. This indicates that A_{1g} mode is strongly sensitive to electron-doping due to the stronger electron-phonon coupling of the A_{1g}-mode [213]. Conversely, with increasing tensile (compressive) strain, the E^1_{2g}-mode is red-shifted (blue-shifted) while the A_{1g}-mode remains unchanged [214, 215]. In the same study involving the 1H-1T′ phase transition of MoS_2 on Au substrate induced by high-temperature annealing [60], both the E^1_{2g} and A_{1g}-modes are red-shifted – an indication of the concurrent increase in both the tensile strain and electron-doping to the monolayer-MoS_2 sample during the phase transition process. Figure 1.26a displays the evolution of both the Raman modes of MoS_2/Au with respect to the annealing temperature and Figure 1.26b,c display the position of the E^1_{2g} and A_{1g}-modes (with MoS_2 on SiO_2 as reference), respectively. The red-shift of the E-mode for MoS_2/Au from ~395 (as-prepared) to ~389 cm^{-1} (250 °C), indicates an increase in tensile strain by ~2.7% after annealing at 250 °C [214, 216]. Meanwhile, there is a redshift of the A_{1g}-mode from ~415 to ~409 cm^{-1} (Figure 1.26c), indicating an increase in electron-doping concentration by more than 1.5×10^{13} cm^{-2} from the Au substrate [57, 213]. Above the optimal annealing

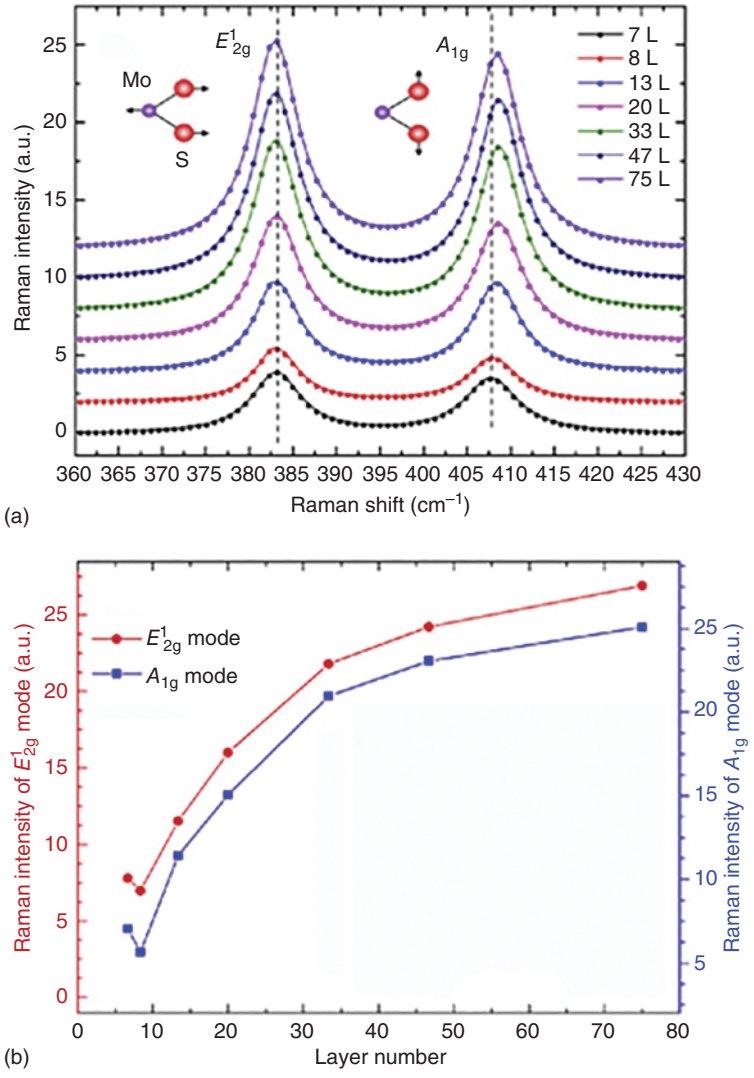

Figure 1.24 Raman profiles of MoS_2 of different thicknesses. (a) Raman spectra of MoS_2 films of different layer number and that of the bulk crystal. (b) Thickness-dependent frequency of E^1_{2g} (in-plane) and A_{1g} modes (out-of-plane) and their difference (right axis). Source: Reproduced with permission from Yuan et al. [204]. © 2016 Acta Materialia Inc. Published by Elsevier Ltd. All rights reserved.

temperature of 250 °C, both the E^1_{2g} and A_{1g}-modes show gradual blue shift as the MoS_2 monolayer begins to undergo thermal decomposition.

These observations are consistent with a previous DFT study which suggested an increase in electron affinity of monolayer-MoS_2 with increasing lattice tensile strain [57]. This has allowed greater charge transfer from the electron-rich Au substrate to the MoS_2 monolayer. Besides, the frequency of both A_{1g} and E-modes can be

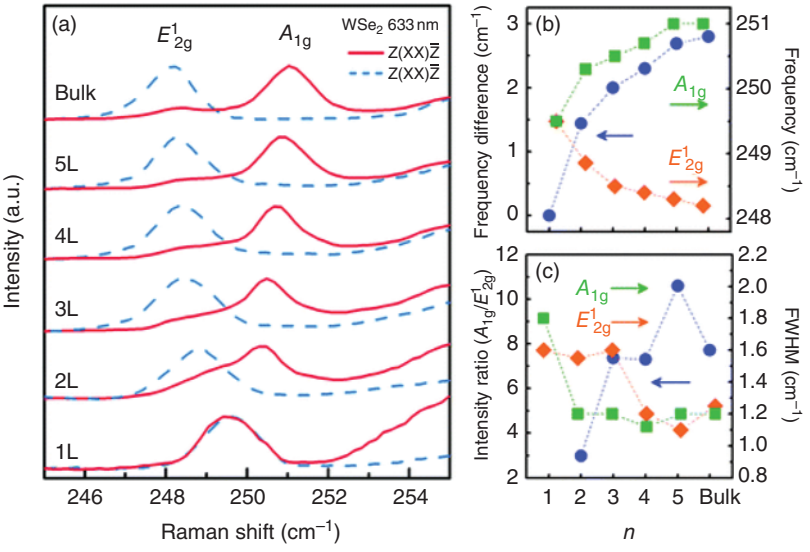

Figure 1.25 Raman profiles of WSe_2 of different thicknesses. (a) Raman spectra of WSe_2 between 1 to 5 layers and in its bulk form. These Raman spectra are obtained in the parallel ($Z(XX)\bar{Z}$) and cross ($Z(XY)\bar{Z}$) polarization conditions. (b) comparing the position of the A_{1g} and E^1_{2g} modes (right vertical axis) and their energy differences (left vertical axis) with respect to layer number. (c) the intensity ratio (left axis) and FWHM (right axis) of the A_{1g} and E^1_{2g} modes with respect to the layer number. Source: Zhao et al. [210]/With permission of Royal Society of Chemistry.

influenced by the presence of structural defects in the MoS_2 monolayer [217]. The frequency of A_{1g}-mode increases alongside a decrease in the frequency of E-mode with increasing lattice defects. However, this does not take place in the experimental observation as presented with increasing annealing temperature. Besides, the FWHM of the A_{1g}-mode ($\sim 5.7\,cm^{-1}$) and E-mode ($\sim 4.6\,cm^{-1}$) of the as-prepared monolayer- MoS_2 are close to those of pristine MoS_2 sample reported previously [217]. Hence, the effects of lattice defects can be ruled out as the main mechanism involved in this annealing-induced phase transition study.

Furthermore, doping-dependent energetics for large-strained (12%) and unstrained MoS_2 (Figure 1.26d) also show that with tensile strain in play, 1T′-phase MoS_2 is energetically favored at smaller electron doping concentrations as compared to one without any lattice strain. This shows that tensile strain and charge-transfer work concurrently to enable the 1H-1T′ phase transition of the 2D-TMD material. The effect of tensile strain facilitating a semiconductor-to-metal phase transition demonstrated recently in thin-film $MoTe_2$ further substantiate this claim [218]. As suggested in previous theoretical studies [219, 220], a system involving monolayer-MoS_2, and the electron-rich Au substrate alone is not a sufficient condition to induce the 1H–1T′ phase transition. This is due to the inefficiency in electron injection attributed to the formation of an interfacial tunnel barrier [219, 220].

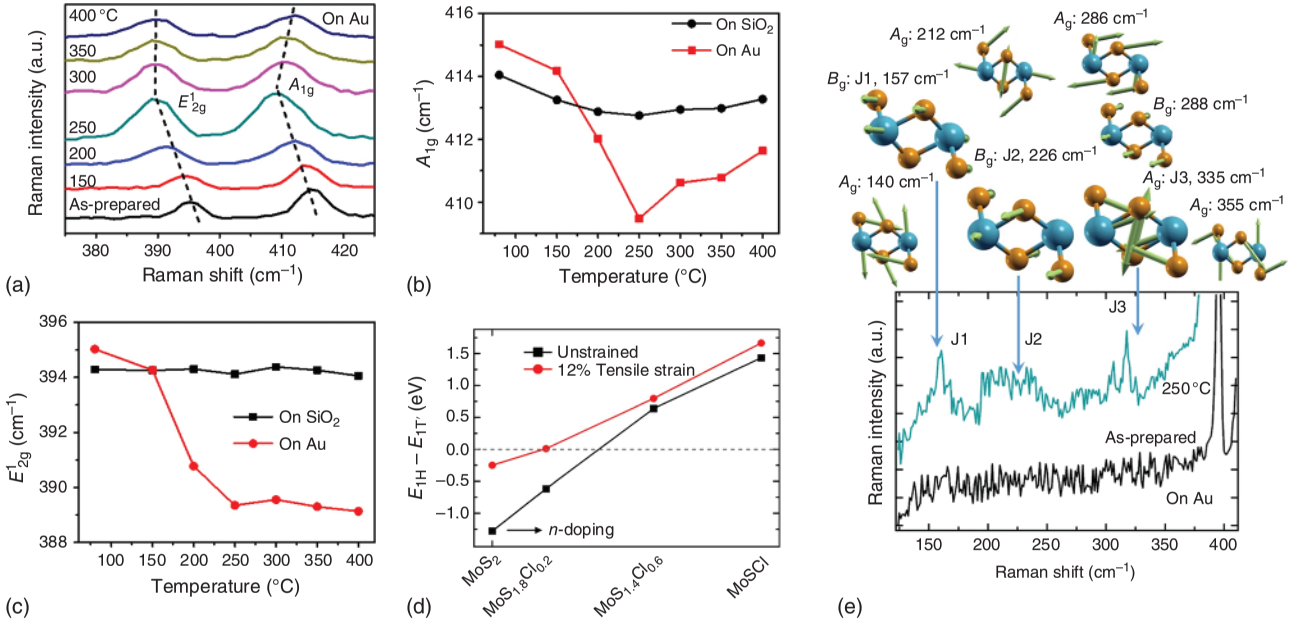

Figure 1.26 (a) Raman spectra of MoS_2/Au at the respective annealing temperatures. Extracted frequencies of (b) A_{1g} and (c) E^1_{2g}-modes as functions of annealing temperature with the respective modes for MoS_2/SiO_2 displayed as reference. The errors of the extracted energy positions are 0.5 cm^{-1}. (d) Calculated energy difference between 1H and 1T′ phases as a function of electron doping concentration for unstrained and strained (12% tensile) monolayer-MoS_2. (e) Top: Calculated Raman active eigenmodes and frequencies, with the corresponding irreducible representation assigned from group theory. Bottom: Comparing Raman spectra of MoS_2/Au before and after annealing at 250 °C. Source: Yin et al. [60]/Springer Nature/Licensed under CC BY 4.0.

Apart from the changes to the E^1_{2g} and the A_{1g} modes during the 1H-1T′ phase transition, there are three main features at ∼157 (J1), ∼224 (J2) and ∼320 cm^{-1} (J3) which can be observed in the Raman spectra of the MoS_2/Au before and after annealing at 250 °C (Figure 1.26e). Distinct to the 1T′-phase [221, 222], these characteristic modes are absent from the semiconducting 1H-phase MoS_2. Besides, they are consistent with published theoretical and experimental studies that show this is the 1T′- rather than 1T-phase MoS_2 [55, 222, 223]. The top of Figure 1.27 displays the calculated Raman active modes and frequencies with their corresponding irreducible representation assigned from group theory of 1T′-phase MoS_2. Most of the experimental peaks correspond to the calculated Raman active eigenmodes.

1.5.3 Electronic Bandgap

Unlike the optical bandgap, the electronic bandgap, and the electronic structures of TMD systems can be characterized using techniques including angle-resolved photoemission spectroscopy (ARPES) and scanning tunneling spectroscopy (STS).

1.5.3.1 Angle-Resolved Photoemission Spectroscopy

As presented in the previous sections, factors including the layer number and the constituent atoms of the TMD materials have long-standing effects on their electronic structures. The effects of the diverse spatial distributions and orbital characters in both the valence and conduction bands previously restricted to mere theoretical calculations can be experimentally verified [225, 226].

ARPES characterization has been employed to investigate the thickness-dependence of the TMD band structure from an indirect to a direct bandgap semiconductor [56, 227, 228]. Owing to the effects of spin-orbit coupling, spin-resolved ARPES has also been involved in unraveling the spin textures of TMD materials [229–231].

Beyond investigating the band structures of TMD systems in their basic forms, ARPES has been utilized to investigate the band structures of TMD heterostructures, charge density waves and superconductivity with a very comprehensive treatment presented in the review [225].

Stacking of TMD monolayers can lead to effects beyond Van der Waals interfacial attraction. A case in point would be the onset of interfacial hybridization in a MoS_2/WSe_2 heterostructure (Figure 1.27) where unique band dispersions can be observed near the Γ-point [224]. Apart from TMD heterostructures, hybrid heterostructures such as MoS_2/graphene have also been investigated using ARPES where Van der Waals interactions result in the modification of the graphene band structure through the formation of several miniband-gaps. This can be attributed to the formation of a super-periodic potential formed by the MoS_2/graphene [232] or the graphene/WS_2 heterostructure [233]. With the immense interest generated by the discovery of superconductivity in “magic-angle” double-layer graphene [234], there is also considerable interest to investigate the effects of periodic Moiré superlattices in TMD heterostructures [235–237]. A case in point would be the evolution of the electronic structures into a highly localized system in the WS_2/WSe_2

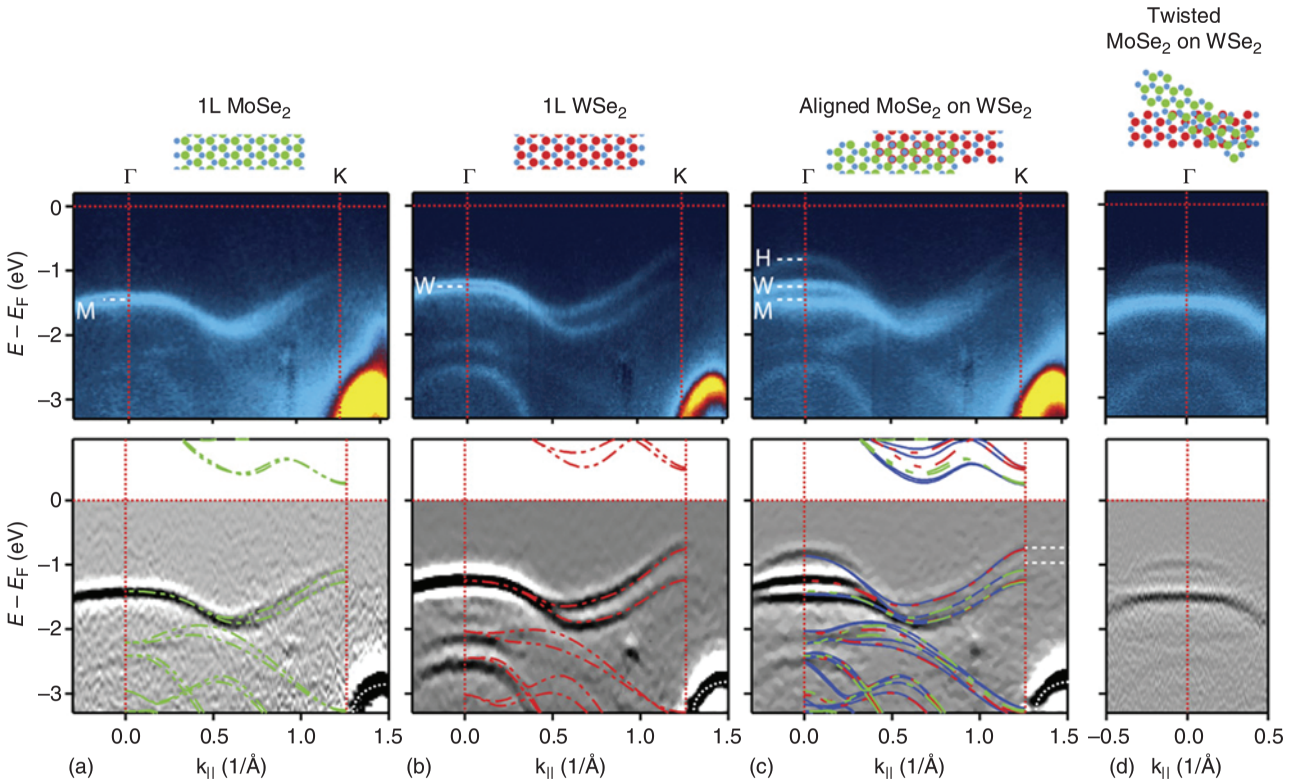

Figure 1.27 Comparing the ARPES-characterized band structures of monolayer and bilayer TMD heterostructures along the Γ–K momentum slices. (a) Band structure of monolayer-$MoSe_2$, (b) monolayer-WSe_2, (c) aligned $MoSe_2/WSe_2$, and (d) $MoSe_2/WSe_2$ heterostructure misaligned at ~30°. While bands near the K-point are very similar between the heterostructures and monolayers – weak interlayer hybridization near K – those at the Γ-point are substantially different, an onset of significant interlayer hybridization for the aligned system (c). Nevertheless, with a misalignment of ~30° between the $MoSe_2$ and WSe_2 layer (d), only two bands are now observed. This suggests that the third band near the Γ-point in the aligned heterostructure arises from commensurate domains. Source: Reproduced with permission from Wilson et al. [224]/American Association for the Advancement of Science/Licensed under CC BY 4.0.

Moiré superlattices with increasingly flat bands and renormalized effective mass. These emerging quantum phases have been monitored using APRES where a large gap opening and splitting exciton peaks have also been observed.

The complex interplay between exotic CDW and superconductive states in various TMD systems are equally intriguing where in some cases, they are found to be co-existing quantum orders [238–241]. ARPES serves as an ideal instrument for the direct observations of both CDW and superconductivity. For the former, Fermi surface reconstruction and folded band structures can be observed due to the enlargement of the lattice unit cells in systems such as $TaSe_2$, $TiSe_2$, VSe_2 and $NbSe_2$ [165, 242–246].

The CDW and superconductive states of 2H-phase $NbSe_2$ are particularly interesting due to their spatial anisotropy and orbital-selective properties [245, 246]. In addition to the anisotropic properties, low-temperature ARPES study has further suggested the role of electron-phonon coupling in dictating the spectral gap and band renormalization. Specifically, the spectral gap consists of two distinct anti-correlated components related to its superconductive and CDW properties [244]. Likewise, layer-dependent effects have also been observed in both the CDW and superconductive states where interlayer interaction and vertical quantum confinement are taken into consideration. For instance, few-layered TMDs have elevated T_{CDW} and weaker superconductivity than their bulk counterparts [232] where multiple theoretical models have been proposed to account for this phenomenon [247, 248].

1.5.3.2 Scanning Tunneling Spectroscopy (STS)

ST measurements have been conducted on a series of mono- and few-layer TMDs on substrates such as highly ordered pyrolytic graphite (HOPG) [164, 249–253] and gold substrates [254]. Comparing similar 2D-TMDs, the measured electronic gap for materials on HOPG tend to be higher than those grown on Au due to the presence of donor states in the latter. An example would be monolayer-MoS_2/HOPG (~2.15 eV) [249] compared to MoS_2/Au (~1.8 eV) [254].

Similar to techniques such as ARPES and PL, STS characterization can be employed to investigate the thickness dependence of TMD materials with the results of MoS_2 [57] (Figure 1.8de), $MoSe_2$ (Figure 1.28) [255] and WSe_2 (Figure 1.29) [253]. The spin texture of the WSe_2 system can be further derived by tracking the series of allowed and forbidden scattering channels with respect to energy. In this case, a large spin-splitting of the valence band can be observed, and this is attributed to the strong spin-orbit coupling. Besides, spin-valley-layer coupling can be observed in the conduction band of bilayer-WSe_2.

As 2D-TMD based semiconductor heterojunctions have also been put under scrutiny using both STS and scanning tunneling microscopy (STM) due to their immense potential for the fabrication of important vertical semiconductor structures and devices. By the detailed examination of the electronic band structures as a result of interfacial lattice strain, band offsets, formation of interfacial states and charge regions, the mechanisms underlying the carrier transport in the heterostructures can be unravelled [256].

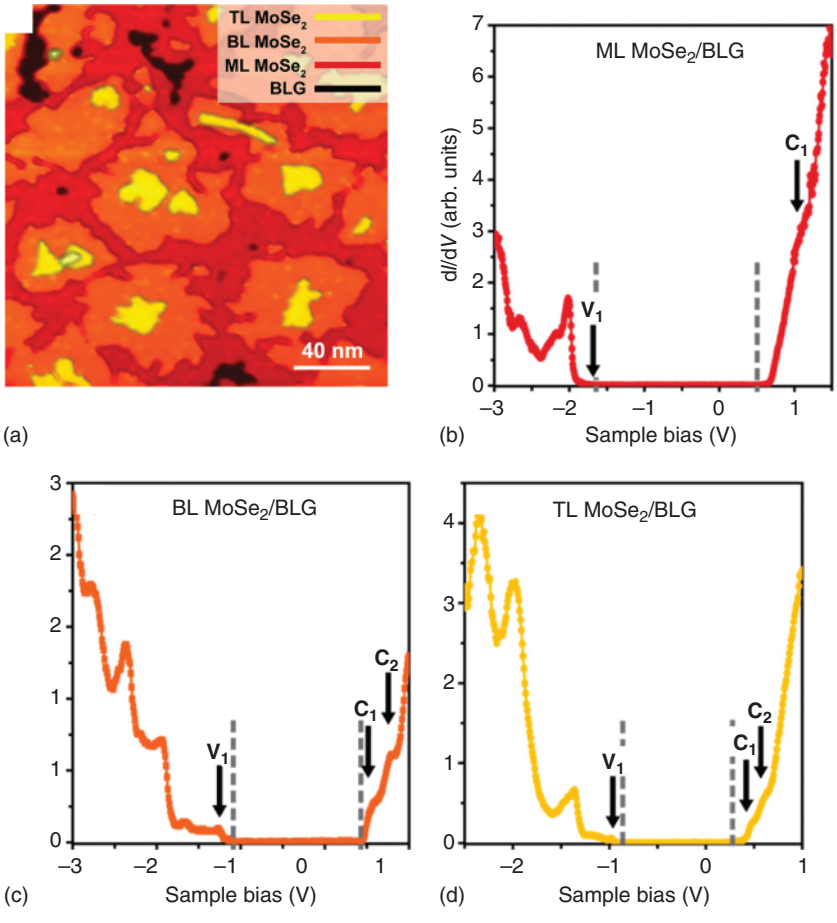

Figure 1.28 STM and STS characterization of mono-, bi- and trilayer $MoSe_2$ synthesized on bilayer graphene (BLG) using MBE. (a) STM image of monolayer-$MoSe_2$/BLG STS spectra for (b) monolayer-$MoSe_2$/BLG (b) bilayer $MoSe_2$/BLG, and (c) trilayer $MoSe_2$/BLG. Source: Reproduced with permission from Bradley et al. [255]/American Chemical Society/Licensed under CC BY 4.0.

The notable example of STM and STS study involving the WSe_2/MoS_2 heterostructure shows that the electronic properties of the bilayer heterostructure change correspondingly with the angle between the layers. Interfacial lattice strain has a direct impact on the system's electronic structures [257]. The band alignment of the vertical WSe_2/MoS_2 heterojunction can be converted from a type II to type I band alignment through lattice strain effects. This strategy involving the epitaxial growth of MoS_2 along the edge of monolayer-WSe_2 induced the strain field only in the MoS_2 region, thereby solely affecting the band structure of monolayer-MoS_2. A similar study can be conducted in the opposite order to examine the impact of lattice strain on monolayer-WSe_2 [256, 257].

The above finding is further substantiated by another study involving the same WSe_2/MoS_2 heterojunction which shows that it is an ideal system for creating a

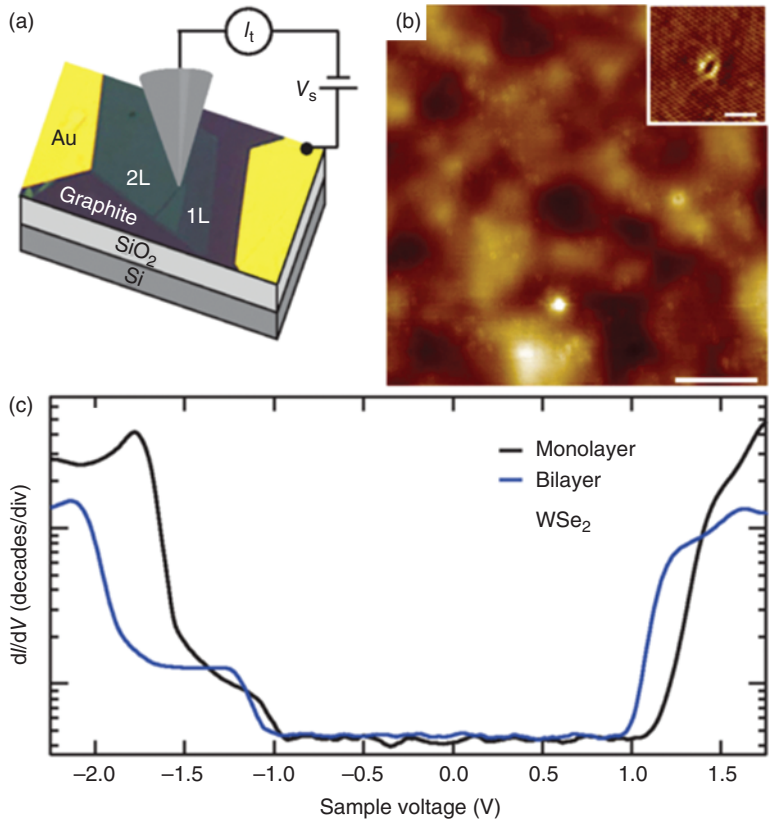

Figure 1.29 STM and STS characterization of WSe_2. (a) Schematic of the system setup to characterize the WSe_2/HOPG sample. (b) STM topography of bilayer-WSe_2. Inset: Atomic resolution of a small lattice defect. (c) d*I*/d*V* spectroscopy of both mono- and bilayer WSe_2. Source: Reproduced with permission from Yankowitz et al. [253]/Reproduced with permission from American Physical Society.

tunable interfacial electrical potential [258]. Such heterostructures can in turn can be utilized in piezoelectric devices [259, 260]. Even in cases where twist angle and lattice mismatch that results in the periodic moiré potentials and structures, the combination of STM and STS measurements can directly probe the magnitude and wavelength of the moiré potential and its electronic structure. A STM study on twisted bilayer-WSe_2 has revealed different localized flat bands between 0° and 60° stacking configureuration [261]. Meanwhile, a separate study on WSe_2/WS_2 has revealed the formation of flat bands near the valence band edge at low temperature [262]. Extensive characterization based on a combination of STM, AFM and TEM measurements has further revealed $MoSe_2/WSe_2$ with a 60° stacking to have a moiré wavelength ranging between 6 – 17 nm at highly symmetrical stacking locations at room temperature [263]. To better understand how the band structure evolves with respect to the moiré pattern and twisted angle, another study involving both STM and STS characterization of $MoSe_2/WSe_2$ hetero-bilayer has revealed a bandgap

modulation between 0° and 60° stacking configureuration [264]. Characterization of local density of states further reveals different localization of electrons between the valence band and conduction band edges [264]. Beyond mere strain effects and mechanical lattice interactions, both STM and STS are effective probing tools to study the impacts of doping [265–268], temperature, structural phase [269–272], edge structure [271–275] on the electronic band structures of TMD heterostructures in both vertical and lateral setups.

1.5.4 Conclusions

This chapter offers a comprehensive overview of 2D-TMDs, their electronic and optical properties that arise due to the diverse polymorphic structures. Multiple experimental techniques have been developed over the years to characterize these unique properties that came about not only due to the structural features, but also intrinsic properties such as spin-orbit coupling. Having established these fundamentals related to 2D-TMDs, the subsequent chapters will further present to readers other important facets of this class of materials pertaining to the theoretical studies, experimental investigations and the potential applications this class of materials promises.

References

1 Novoselov, K.S., Geim, A.K., Morozov, S.V. et al. (2004). Electric field effect in atomically thin carbon films. *Science* 306: 666–669. https://doi.org/10.1126/science.1102896.

2 Frindt, R.F. (1966). Single crystals of MoS_2 several molecular layers thick. *J. Appl. Phys.* 37: 1928–1929. https://doi.org/10.1063/1.1708627.

3 Novoselov, K.S., Jiang, D., Schedin, F. et al. (2005). Two-dimensional atomic crystals. *Proc. Natl. Acad. Sci.* 102: 10451–10453. https://doi.org/10.1073/pnas.0502848102.

4 Wang, Q.H., Kalantar-Zadeh, K., Kis, A. et al. (2012). Electronics and optoelectronics of two-dimensional transition metal dichalcogenides. *Nat. Nanotechnol.* 7: 699–712. https://doi.org/10.1038/nnano.2012.193.

5 Xu, X., Yao, W., Xiao, D., and Heinz, T.F. (2014). Spin and pseudospins in layered transition metal dichalcogenides. *Nat. Phys.* 10: 343–350. https://doi.org/10.1038/nphys2942.

6 Xia, F., Wang, H., Xiao, D. et al. (2014). Two-dimensional material nanophotonics. *Nat. Photonics* 8: 899–907. https://doi.org/10.1038/nphoton.2014.271.

7 Eda, G., Fujita, T., Yamaguchi, H. et al. (2012). Coherent atomic and electronic heterostructures of single-layer MoS_2. *ACS Nano* 6: 7311–7317. https://doi.org/10.1021/nn302422x.

8 Qian, X., Liu, J., Fu, L., and Li, J. (2014). Quantum spin hall effect in two-dimensional transition metal dichalcogenides. *Science* 346: 1344–1347. https://doi.org/10.1126/science.1256815.

9 Keum, D.H., Cho, S., Kim, J.H. et al. (2015). Bandgap opening in few-layered monoclinic $MoTe_2$. *Nat. Phys.* 11: 482–486. https://doi.org/10.1038/nphys3314.

10 Calandra, M. (2013). Chemically exfoliated single-layer Mos_2: stability, lattice dynamics, and catalytic adsorption from first principles. *Phys. Rev., B* 88: 245428. https://doi.org/10.1103/PhysRevB.88.245428.

11 Tang, C.S., Yin, X., and Wee, A.T.S. (2021). 1D chain structure in 1T′-phase 2D transition metal dichalcogenides and their anisotropic electronic structures. *Appl. Phys. Rev.* 8: 011313. https://doi.org/10.1063/5.0023799.

12 Porer, M., Leierseder, U., Ménard, J.M. et al. (2014). Non-thermal separation of electronic and structural orders in a persisting charge density wave. *Nat. Mater.* 13: 857–861. https://doi.org/10.1038/nmat4042.

13 Liu, G., Debnath, B., Pope, T.R. et al. (2016). A charge-density-wave oscillator based on an integrated tantalum disulfide–boron nitride–graphene device operating at room temperature. *Nat. Nanotechnol.* 11: 845–850. https://doi.org/10.1038/nnano.2016.108.

14 Geremew, A.K., Rumyantsev, S., Kargar, F. et al. (2019). Bias-voltage driven switching of the charge-density-wave and normal metallic phases in 1T-TaS_2 thin-film devices. *ACS Nano* 13: 7231–7240. https://doi.org/10.1021/acsnano.9b02870.

15 Geremew, A.K., Kargar, F., Zhang, E.X. et al. (2019). Proton-irradiation-immune electronics implemented with two-dimensional charge-density-wave devices. *Nanoscale* 11: 8380–8386. https://doi.org/10.1039/C9NR01614G.

16 Kadantsev, E.S. and Hawrylak, P. (2012). Electronic structure of a single MoS_2 monolayer. *Solid State Commun.* 152: 909–913. https://doi.org/10.1016/j.ssc.2012.02.005.

17 Wilson, J.A., Di Salvo, F.J., and Mahajan, S. (1975). Charge-density waves and superlattices in the metallic layered transition metal dichalcogenides. *Adv. Phys.* 24: 117–201. https://doi.org/10.1080/00018737500101391.

18 Moncton, D.E., Axe, J.D., and DiSalvo, F.J. (1975). Study of superlattice formation in 2H-$NbSe_2$ and 2H-$TaSe_2$ by neutron scattering. *Phys. Rev. Lett.* 34: 734–737. https://doi.org/10.1103/PhysRevLett.34.734.

19 Fazekas, P. and Tosatti, E. (1979). Electrical, structural and magnetic properties of pure and doped 1T-TaS_2. *Philos. Mag. B* 39: 229–244. https://doi.org/10.1080/13642817908245359.

20 Sipos, B., Kusmartseva, A.F., Akrap, A. et al. (2008). From Mott state to superconductivity in 1T-TaS_2. *Nat. Mater.* 7: 960–965. https://doi.org/10.1038/nmat2318.

21 Tsen, A.W., Hovden, R., Wang, D. et al. (2015). Structure and control of charge density waves in two-dimensional 1T-TaS_2. *Proc. Natl. Acad. Sci.* 112: 15054–15059. https://doi.org/10.1073/pnas.1512092112.

22 Sun, Y., Wu, S.-C., Ali, M.N. et al. (2015). Prediction of Weyl semimetal in orthorhombic $MoTe_2$. *Phys. Rev., B* 92: 161107. https://doi.org/10.1103/PhysRevB.92.161107.

23 Ali, M.N., Xiong, J., Flynn, S. et al. (2014). Large, non-saturating magnetoresistance in WTe_2. *Nature* 514: 205–208. https://doi.org/10.1038/nature13763.

24 Ma, F., Gao, G., Jiao, Y. et al. (2016). Predicting a new phase (T′′) of two-dimensional transition metal di-chalcogenides and strain-controlled topological phase transition. *Nanoscale* 8: 4969–4975. https://doi.org/10.1039/C5NR07715J.

25 Heising, J. and Kanatzidis, M.G. (1999). Structure of restacked MoS_2 and WS_2 elucidated by electron crystallography. *J. Am. Chem. Soc.* 121: 638–643. https://doi.org/10.1021/ja983043c.

26 Heising, J. and Kanatzidis, M.G. (1999). Exfoliated and restacked MoS_2 and WS_2: ionic or neutral species? Encapsulation and ordering of hard electropositive cations. *J. Am. Chem. Soc.* 121: 11720–11732. https://doi.org/10.1021/ja991644d.

27 Bruyer, E., Di Sante, D., Barone, P. et al. (2016). Possibility of combining ferroelectricity and Rashba-like spin splitting in monolayers of the 1T-type transition-metal dichalcogenides MX_2(M=Mo,W;X=S,Se,Te). *Phys. Rev., B* 94: 195402. https://doi.org/10.1103/PhysRevB.94.195402.

28 Zhuang, H.L., Johannes, M.D., Singh, A.K., and Hennig, R.G. (2017). Doping-controlled phase transitions in single-layer MoS_2. *Phys. Rev., B* 96: 165305. https://doi.org/10.1103/PhysRevB.96.165305.

29 Li, Y., Duerloo, K.-A.N., Wauson, K., and Reed, E.J. (2016). Structural semiconductor-to-semimetal phase transition in two-dimensional materials induced by electrostatic gating. *Nat. Commun.* 7: 10671. https://doi.org/10.1038/ncomms10671.

30 Duerloo, K.-A.N., Li, Y., and Reed, E.J. (2014). Structural phase transitions in two-dimensional Mo- and W-dichalcogenide monolayers. *Nat. Commun.* 5: 4214. https://doi.org/10.1038/ncomms5214.

31 Santhosh, K.C., Zhang, C., Hong, S. et al. (2015). Phase stability of transition metal dichalcogenide by competing ligand field stabilization and charge density wave. *2D Materials* 2: 035019. https://doi.org/10.1088/2053-1583/2/3/035019.

32 Kan, M., Nam, H.G., Lee, Y.H., and Sun, Q. (2015). Phase stability and Raman vibration of the molybdenum ditelluride ($MoTe_2$) monolayer. *Phys. Chem. Chem. Phys.* 17: 14866–14871. https://doi.org/10.1039/C5CP01649E.

33 Ataca, C., Şahin, H., and Ciraci, S. (2012). Stable, single-layer MX_2 transition-metal oxides and dichalcogenides in a honeycomb-like structure. *J. Phys. Chem., C* 116: 8983–8999. https://doi.org/10.1021/jp212558p.

34 Bertolazzi, S., Brivio, J., and Kis, A. (2011). Stretching and breaking of ultrathin MoS_2. *ACS Nano* 5: 9703–9709. https://doi.org/10.1021/nn203879f.

35 Cooper, R.C., Lee, C., Marianetti, C.A. et al. (2013). Nonlinear elastic behavior of two-dimensional molybdenum disulfide. *Phys. Rev., B* 87: 035423. https://doi.org/10.1103/PhysRevB.87.035423.

36 Miró, P., Ghorbani-Asl, M., and Heine, T. (2013). Spontaneous ripple formation in MoS_2 monolayers: electronic structure and transport effects. *Adv. Mater.* 25: 5473–5475. https://doi.org/10.1002/adma.201301492.

37 Singh, S.K., Neek-Amal, M., Costamagna, S., and Peeters, F.M. (2015). Rippling, buckling, and melting of single- and multilayer MoS_2. *Phys. Rev., B* 91: 014101. https://doi.org/10.1103/PhysRevB.91.014101.

38 Lebègue, S. and Eriksson, O. (2009). Electronic structure of two-dimensional crystals from ab initio theory. *Phys. Rev., B* 79: 115409. https://doi.org/10.1103/PhysRevB.79.115409.

39 Ding, Y., Wang, Y., Ni, J. et al. (2011). First principles study of structural, vibrational and electronic properties of graphene-like MX_2 (M=Mo, Nb, W, Ta; X=S, Se, Te) monolayers. *Physica B* 406: 2254–2260. https://doi.org/10.1016/j.physb.2011.03.044.

40 Dawson, W.G. and Bullett, D.W. (1987). Electronic structure and crystallography of $MoTe_2$ and WTe_2. *J. Phys. C: Solid State Phys.* 20: 6159–6174. https://doi.org/10.1088/0022-3719/20/36/017.

41 Augustin, J., Eyert, V., Böker, T. et al. (2000). Electronic band structure of the layered compound Td–WTe_2. *Phys. Rev., B* 62: 10812–10823. https://doi.org/10.1103/PhysRevB.62.10812.

42 Zeng, Z., Yin, Z., Huang, X. et al. (2011). Single-layer semiconducting nanosheets: high-yield preparation and device fabrication. *Angew. Chem. Int. Ed.* 50: 11093–11097. https://doi.org/10.1002/anie.201106004.

43 Tongay, S., Sahin, H., Ko, C. et al. (2014). Monolayer behaviour in bulk ReS_2 due to electronic and vibrational decoupling. *Nat. Commun.* 5: 3252. https://doi.org/10.1038/ncomms4252.

44 Böker, T., Severin, R., Müller, A. et al. (2001). Band structure of MoS_2 $MoSe_2$ and alpha-$MoTe_2$ angle-resolved photoelectron spectroscopy and ab initio calculations. *Phys. Rev., B* 64: 235305. https://doi.org/10.1103/PhysRevB.64.235305.

45 Wilson, J.A. and Yoffe, A.D. (1969). The transition metal dichalcogenides discussion and interpretation of the observed optical, electrical and structural properties. *Adv. Phys.* 18: 193–335. https://doi.org/10.1080/00018736900101307.

46 Ribeiro-Soares, J., Almeida, R.M., Barros, E.B. et al. (2014). Group theory analysis of phonons in two-dimensional transition metal dichalcogenides. *Phys. Rev., B* 90: 115438. https://doi.org/10.1103/PhysRevB.90.115438.

47 Roldán, R., Silva-Guillén, J.A., López-Sancho, M.P. et al. (2014). Electronic properties of single-layer and multilayer transition metal dichalcogenides MX_2 (M = Mo, W and X = S, Se). *Ann. Phys.* 526: 347–357. https://doi.org/10.1002/andp.201400128.

48 Yun, W.S., Han, S.W., Hong, S.C. et al. (2012). Thickness and strain effects on electronic structures of transition metal dichalcogenides: 2H-MX_2 semiconductors (M = Mo, W; X = S, Se, Te). *Phys. Rev., B* 85: 033305. https://doi.org/10.1103/PhysRevB.85.033305.

49 Zhao, W., Ribeiro, R.M., Toh, M. et al. (2013). Origin of indirect optical transitions in few-layer MoS_2, WS_2, and WSe_2. *Nano Lett.* 13: 5627–5634. https://doi.org/10.1021/nl403270k.

50 Zhu, Z.Y., Cheng, Y.C., and Schwingenschlögl, U. (2011). Giant spin-orbit-induced spin splitting in two-dimensional transition-metal dichalcogenide semiconductors. *Phys. Rev., B* 84: 153402. https://doi.org/10.1103/PhysRevB.84.153402.

51 Li, T. and Galli, G. (2007). Electronic properties of MoS_2 nanoparticles. *J. Phys. Chem., C* 111: 16192–16196. https://doi.org/10.1021/jp075424v.

52 Kormányos, A., Burkard, G., Gmitra, M. et al. (2015). k · p theory for two-dimensional transition metal dichalcogenide semiconductors. *2D Materials* 2: 022001. https://doi.org/10.1088/2053-1583/2/2/022001.

53 Mak, K.F., Lee, C., Hone, J. et al. (2010). Atomically thin MoS_2: a new direct-gap semiconductor. *Phys. Rev. Lett.* 105: 136805. https://doi.org/10.1103/PhysRevLett.105.136805.

54 Splendiani, A., Sun, L., Zhang, Y. et al. (2010). Emerging photoluminescence in monolayer MoS_2. *Nano Lett.* 10: 1271–1275. https://doi.org/10.1021/nl903868w.

55 Hu, T., Li, R., and Dong, J. (2013). A new (2 × 1) dimerized structure of monolayer 1T-molybdenum disulfide, studied from first principles calculations. *J. Chem. Phys.* 139: 174702. https://doi.org/10.1063/1.4827082.

56 Jin, W., Yeh, P.-C., Zaki, N. et al. (2013). Direct measurement of the thickness-dependent electronic band structure of MoS_2 using angle-resolved photoemission spectroscopy. *Phys. Rev. Lett.* 111: 106801. https://doi.org/10.1103/PhysRevLett.111.106801.

57 Huang, Y.L., Chen, Y., Zhang, W. et al. (2015). Bandgap tunability at single-layer molybdenum disulphide grain boundaries. *Nat. Commun.* 6: 6298. https://doi.org/10.1038/ncomms7298.

58 Ugeda, M.M., Pulkin, A., Tang, S. et al. (2018). Observation of topologically protected states at crystalline phase boundaries in single-layer WSe_2. *Nat. Commun.* 9: 3401. https://doi.org/10.1038/s41467-018-05672-w.

59 Tang, S., Zhang, C., Wong, D. et al. (2017). Quantum spin hall state in monolayer 1T'-WTe_2. *Nat. Phys.* 13: 683–687. https://doi.org/10.1038/nphys4174.

60 Yin, X., Wang, Q., Cao, L. et al. (2017). Tunable inverted gap in monolayer quasi-metallic MoS_2 induced by strong charge-lattice coupling. *Nat. Commun.* 8: 486. https://doi.org/10.1038/s41467-017-00640-2.

61 Tang, C.S., Yin, X., Yang, M. et al. (2020). Anisotropic collective charge excitations in quasimetallic 2D transition-metal dichalcogenides. *Adv. Sci.* 7: 1902726. https://doi.org/10.1002/advs.201902726.

62 Kuc, A., Zibouche, N., and Heine, T. (2011). Influence of quantum confinement on the electronic structure of the transition metal sulfide T_2. *Phys. Rev., B* 83: 245213. https://doi.org/10.1103/PhysRevB.83.245213.

63 Ramakrishna Matte, H.S.S., Gomathi, A., Manna, A.K. et al. (2010). MoS_2 and WS_2 analogues of graphene. *Angew. Chem. Int. Ed.* 49: 4059–4062. https://doi.org/10.1002/anie.201000009.

64 Radisavljevic, B., Radenovic, A., Brivio, J. et al. (2011). Single-layer MoS_2 transistors. *Nat. Nanotechnol.* 6: 147–150. https://doi.org/10.1038/nnano.2010.279.

65 Voß, D., Krüger, P., Mazur, A., and Pollmann, J. (1999). Atomic and electronic structure of WSe_2 from ab initio theory: bulk crystal and thin film systems. *Phys. Rev., B* 60: 14311–14317. https://doi.org/10.1103/PhysRevB.60.14311.

66 Bonaccorso, F., Bartolotta, A., Coleman, J.N., and Backes, C. (2016). 2D-crystal-based functional inks. *Adv. Mater.* 28: 6136–6166. https://doi.org/10.1002/adma.201506410.

67 Hill, H.M., Rigosi, A.F., Rim, K.T. et al. (2016). Band alignment in MoS_2/WS_2 transition metal dichalcogenide heterostructures probed by scanning tunneling

microscopy and spectroscopy. *Nano Lett.* 16: 4831–4837. https://doi.org/10.1021/acs.nanolett.6b01007.

68 Wickramaratne, D., Zahid, F., and Lake, R.K. (2014). Electronic and thermoelectric properties of few-layer transition metal dichalcogenides. *J. Chem. Phys.* 140: 124710. https://doi.org/10.1063/1.4869142.

69 Wang, G., Chernikov, A., Glazov, M.M. et al. (2018). Colloquium: excitons in atomically thin transition metal dichalcogenides. *Rev. Mod. Phys.* 90: 021001. https://doi.org/10.1103/RevModPhys.90.021001.

70 Herman, F., Kuglin, C.D., Cuff, K.F., and Kortum, R.L. (1963). Relativistic corrections to the band structure of tetrahedrally bonded semiconductors. *Phys. Rev. Lett.* 11: 541–545. https://doi.org/10.1103/PhysRevLett.11.541.

71 Tang, C.S., Yin, X., Yang, M. et al. (2019). Three-dimensional resonant exciton in monolayer tungsten diselenide actuated by spin–orbit coupling. *ACS Nano* 13: 14529–14539. https://doi.org/10.1021/acsnano.9b08385.

72 Cheiwchanchamnangij, T. and Lambrecht, W.R.L. (2012). Quasiparticle band structure calculation of monolayer, bilayer, and bulk MoS_2. *Phys. Rev., B* 85: 205302. https://doi.org/10.1103/PhysRevB.85.205302.

73 Xiao, D., Liu, G.-B., Feng, W. et al. (2012). Coupled spin and valley physics in monolayers of MoS_2 and other group-VI dichalcogenides. *Phys. Rev. Lett.* 108: 196802. https://doi.org/10.1103/PhysRevLett.108.196802.

74 Zhang, Y., Chang, T.-R., Zhou, B. et al. (2014). Direct observation of the transition from indirect to direct bandgap in atomically thin epitaxial $MoSe_2$. *Nat. Nanotechnol.* 9: 111–115. https://doi.org/10.1038/nnano.2013.277.

75 Miwa, J.A., Ulstrup, S., Sørensen, S.G. et al. (2015). Electronic structure of epitaxial single-layer MoS_2. *Phys. Rev. Lett.* 114: 046802. https://doi.org/10.1103/PhysRevLett.114.046802.

76 Kośmider, K., González, J.W., and Fernández-Rossier, J. (2013). Large spin splitting in the conduction band of transition metal dichalcogenide monolayers. *Phys. Rev., B* 88: 245436. https://doi.org/10.1103/PhysRevB.88.245436.

77 Liu, G.-B., Shan, W.-Y., Yao, Y. et al. (2013). Three-band tight-binding model for monolayers of group-VIB transition metal dichalcogenides. *Phys. Rev., B* 88: 085433. https://doi.org/10.1103/PhysRevB.88.085433.

78 Kormányos, A., Zólyomi, V., Drummond, N.D., and Burkard, G. (2014). Spin-orbit coupling, quantum dots, and qubits in monolayer transition metal dichalcogenides. *Phys. Rev. X* 4: 011034. https://doi.org/10.1103/PhysRevX.4.011034.

79 Dery, H. and Song, Y. (2015). Polarization analysis of excitons in monolayer and bilayer transition-metal dichalcogenides. *Phys. Rev., B* 92: 125431. https://doi.org/10.1103/PhysRevB.92.125431.

80 Qiu, D.Y., Cao, T., and Louie, S.G. (2015). Nonanalyticity, valley quantum phases, and lightlike exciton dispersion in monolayer transition metal dichalcogenides: theory and first-principles calculations. *Phys. Rev. Lett.* 115: 176801. https://doi.org/10.1103/PhysRevLett.115.176801.

81 Echeverry, J.P., Urbaszek, B., Amand, T. et al. (2016). Splitting between bright and dark excitons in transition metal dichalcogenide monolayers. *Phys. Rev., B* 93: 121107. https://doi.org/10.1103/PhysRevB.93.121107.

82 Wang, G., Robert, C., Suslu, A. et al. (2015). Spin-orbit engineering in transition metal dichalcogenide alloy monolayers. *Nat. Commun.* 6: 10110. https://doi.org/10.1038/ncomms10110.

83 Zhang, X.-X., You, Y., Zhao, S.Y.F., and Heinz, T.F. (2015). Experimental evidence for dark excitons in monolayer WSe_2. *Phys. Rev. Lett.* 115: 257403. https://doi.org/10.1103/PhysRevLett.115.257403.

84 Arora, A., Koperski, M., Nogajewski, K. et al. (2015). Excitonic resonances in thin films of WSe_2: from monolayer to bulk material. *Nanoscale* 7: 10421–10429. https://doi.org/10.1039/C5NR01536G.

85 Withers, F., Del Pozo-Zamudio, O., Schwarz, S. et al. (2015). WSe_2 light-emitting tunneling transistors with enhanced brightness at room temperature. *Nano Lett.* 15: 8223–8228. https://doi.org/10.1021/acs.nanolett.5b03740.

86 Zhang, X.-X., Cao, T., Lu, Z. et al. (2017). Magnetic brightening and control of dark excitons in monolayer WSe_2. *Nat. Nanotechnol.* 12: 883–888. https://doi.org/10.1038/nnano.2017.105.

87 Yao, W., Xiao, D., and Niu, Q. (2008). Valley-dependent optoelectronics from inversion symmetry breaking. *Phys. Rev., B* 77: 235406. https://doi.org/10.1103/PhysRevB.77.235406.

88 Zeng, H., Dai, J., Yao, W. et al. (2012). Valley polarization in MoS_2 monolayers by optical pumping. *Nat. Nanotechnol.* 7: 490–493. https://doi.org/10.1038/nnano.2012.95.

89 Sallen, G., Bouet, L., Marie, X. et al. (2012). Robust optical emission polarization in MoS_2 monolayers through selective valley excitation. *Phys. Rev., B* 86: 081301. https://doi.org/10.1103/PhysRevB.86.081301.

90 Cao, T., Wang, G., Han, W. et al. (2012). Valley-selective circular dichroism of monolayer molybdenum disulphide. *Nat. Commun.* 3: 887. https://doi.org/10.1038/ncomms1882.

91 Pacchioni, G. (2020). Valleytronics with a twist. *Nat. Rev. Mater.* 5: 480–480. https://doi.org/10.1038/s41578-020-0220-2.

92 Mak, K.F., Xiao, D., and Shan, J. (2018). Light–valley interactions in 2D semiconductors. *Nat. Photonics* 12: 451–460. https://doi.org/10.1038/s41566-018-0204-6.

93 Schaibley, J.R., Yu, H., Clark, G. et al. (2016). Valleytronics in 2D materials. *Nat. Rev. Mater.* 1: 16055. https://doi.org/10.1038/natrevmats.2016.55.

94 Knox, R.S. (1983). Introduction to exciton physics. In: *Collective Excitations in Solids* (ed. B. Di Bartolo), 183–245. US: Springer.

95 Nam, S.B., Reynolds, D.C., Litton, C.W. et al. (1976). Free-exciton energy spectrum in GaAs. *Phys. Rev., B* 13: 761–767. https://doi.org/10.1103/PhysRevB.13.761.

96 Kazimierczuk, T., Fröhlich, D., Scheel, S. et al. (2014). Giant Rydberg excitons in the copper oxide Cu_2O. *Nature* 514: 343–347. https://doi.org/10.1038/nature13832.

97 Wannier, G.H. (1937). The structure of electronic excitation levels in insulating crystals. *Phys. Rev.* 52: 191–197. https://doi.org/10.1103/PhysRev.52.191.

98 Aldrich, C. and Bajaj, K.K. (1977). Binding energy of a Mott-Wannier exciton in a polarizable medium. *Solid State Commun.* 22: 157–160. https://doi.org/10.1016/0038-1098(77)90423-9.

99 Hjalmarson, H.P., Büttner, H., and Dow, J.D. (1981). Theory of core excitons. *Phys. Rev., B* 24: 6010–6019. https://doi.org/10.1103/PhysRevB.24.6010.

100 Stein, T., Kronik, L., and Baer, R. (2009). Reliable prediction of charge transfer excitations in molecular complexes using time-dependent density functional theory. *J. Am. Chem. Soc.* 131: 2818–2820. https://doi.org/10.1021/ja8087482.

101 Cho, S.W., Piper, L.F.J., DeMasi, A. et al. (2010). Electronic structure of C60/phthalocyanine/ITO interfaces studied using soft X-ray spectroscopies. *J. Phys. Chem., C* 114: 1928–1933. https://doi.org/10.1021/jp910504a.

102 Arkhipov, V.I. and Bässler, H. (2004). Exciton dissociation and charge photogeneration in pristine and doped conjugated polymers. *Phys. Status Solidi A* 201: 1152–1187. https://doi.org/10.1002/pssa.200404339.

103 Stier, A.V., Wilson, N.P., Clark, G. et al. (2016). Probing the influence of dielectric environment on excitons in monolayer WSe_2: insight from high magnetic fields. *Nano Lett.* 16: 7054–7060. https://doi.org/10.1021/acs.nanolett.6b03276.

104 Cadiz, F., Courtade, E., Robert, C. et al. (2017). Excitonic linewidth approaching the homogeneous limit in MoS_2-based van der Waals heterostructures. *Phys. Rev. X* 7: 021026. https://doi.org/10.1103/PhysRevX.7.021026.

105 Raja, A., Chaves, A., Yu, J. et al. (2017). Coulomb engineering of the bandgap and excitons in two-dimensional materials. *Nat. Commun.* 8: 15251. https://doi.org/10.1038/ncomms15251.

106 He, X.-F. (1991). Excitons in anisotropic solids: the model of fractional-dimensional space. *Phys. Rev., B* 43: 2063–2069. https://doi.org/10.1103/PhysRevB.43.2063.

107 Chernikov, A., Berkelbach, T.C., Hill, H.M. et al. (2014). Exciton binding energy and nonhydrogenic rydberg series in monolayer WS_2. *Phys. Rev. Lett.* 113: 076802. https://doi.org/10.1103/PhysRevLett.113.076802.

108 Berkelbach, T.C., Hybertsen, M.S., and Reichman, D.R. (2013). Theory of neutral and charged excitons in monolayer transition metal dichalcogenides. *Phys. Rev., B* 88: 045318. https://doi.org/10.1103/PhysRevB.88.045318.

109 Feng, J., Qian, X., Huang, C.-W., and Li, J. (2012). Strain-engineered artificial atom as a broad-spectrum solar energy funnel. *Nat. Photonics* 6: 866–872. https://doi.org/10.1038/nphoton.2012.285.

110 Qiu, D.Y., da Jornada, F.H., and Louie, S.G. (2013). Optical spectrum of MoS_2: many-body effects and diversity of exciton states. *Phys. Rev. Lett.* 111: 216805. https://doi.org/10.1103/PhysRevLett.111.216805.

111 Molina-Sánchez, A., Sangalli, D., Hummer, K. et al. (2013). Effect of spin-orbit interaction on the optical spectra of single-layer, double-layer, and bulk MoS_2. *Phys. Rev., B* 88: 045412. https://doi.org/10.1103/PhysRevB.88.045412.

112 Mak, K.F., He, K., Lee, C. et al. (2013). Tightly bound trions in monolayer MoS_2. *Nat. Mater.* 12: 207–211. https://doi.org/10.1038/nmat3505.

113 Gogoi, P.K., Hu, Z., Wang, Q. et al. (2017). Oxygen passivation mediated tunability of trion and excitons in MoS_2. *Phys. Rev. Lett.* 119: 077402. https://doi.org/10.1103/PhysRevLett.119.077402.

114 Thilagam, A. (2014). Exciton complexes in low dimensional transition metal dichalcogenides. *J. Appl. Phys.* 116: 053523. https://doi.org/10.1063/1.4892488.

115 You, Y., Zhang, X.-X., Berkelbach, T.C. et al. (2015). Observation of biexcitons in monolayer WSe_2. *Nat. Phys.* 11: 477–481. https://doi.org/10.1038/nphys3324.

116 Klingshirn, C.F. (2007). *Semiconductor Optics*, vol. 3. Springer.

117 Cudazzo, P., Tokatly, I.V., and Rubio, A. (2011). Dielectric screening in two-dimensional insulators: implications for excitonic and impurity states in graphane. *Phys. Rev., B* 84: 085406. https://doi.org/10.1103/PhysRevB.84.085406.

118 Ross, J.S., Wu, S., Yu, H. et al. (2013). Electrical control of neutral and charged excitons in a monolayer semiconductor. *Nat. Commun.* 4: 1474. https://doi.org/10.1038/ncomms2498.

119 Huard, V., Cox, R.T., Saminadayar, K. et al. (2000). Bound states in optical absorption of semiconductor quantum wells containing a two-dimensional electron gas. *Phys. Rev. Lett.* 84: 187–190. https://doi.org/10.1103/PhysRevLett.84.187.

120 Albrecht, S., Reining, L., Del Sole, R., and Onida, G. (1998). Ab initio calculation of excitonic effects in the optical spectra of semiconductors. *Phys. Rev. Lett.* 80: 4510–4513. https://doi.org/10.1103/PhysRevLett.80.4510.

121 Rohlfing, M. and Louie, S.G. (1998). Electron-hole excitations in semiconductors and insulators. *Phys. Rev. Lett.* 81: 2312–2315. https://doi.org/10.1103/PhysRevLett.81.2312.

122 Yang, L., Deslippe, J., Park, C.-H. et al. (2009). Excitonic effects on the optical response of graphene and bilayer graphene. *Phys. Rev. Lett.* 103: 186802. https://doi.org/10.1103/PhysRevLett.103.186802.

123 Mak, K.F., Shan, J., and Heinz, T.F. (2011). Seeing many-body effects in single- and few-layer graphene: observation of two-dimensional saddle-point excitons. *Phys. Rev. Lett.* 106: 046401. https://doi.org/10.1103/PhysRevLett.106.046401.

124 Zhang, Q., Jie, J., Diao, S. et al. (2015). Solution-processed graphene quantum dot deep-UV photodetectors. *ACS Nano* 9: 1561–1570. https://doi.org/10.1021/acsnano.5b00437.

125 Zeng, L., Tao, L., Tang, C. et al. (2016). High-responsivity UV-vis photodetector based on transferable WS_2 film deposited by magnetron sputtering. *Sci. Rep.* 6: 20343. https://doi.org/10.1038/srep20343.

126 Singh, R.S., Li, D., Xiong, Q. et al. (2016). Anomalous photoresponse in the deep-ultraviolet due to resonant excitonic effects in oxygen plasma treated few-layer graphene. *Carbon* 106: 330–335. https://doi.org/10.1016/j.carbon.2016.05.026.

127 Yang, L. (2011). Excitons in intrinsic and bilayer graphene. *Phys. Rev., B* 83: 085405. https://doi.org/10.1103/PhysRevB.83.085405.

128 Benameur, M.M., Radisavljevic, B., Héron, J.S. et al. (2011). Visibility of dichalcogenide nanolayers. *Nanotechnology* 22: 125706. https://doi.org/10.1088/0957-4484/22/12/125706.

129 Coleman, J.N., Lotya, M., O'Neill, A. et al. (2011). Two-dimensional nanosheets produced by liquid exfoliation of layered materials. *Science* 331: 568–571. https://doi.org/10.1126/science.1194975.

130 Nicolosi, V., Chhowalla, M., Kanatzidis, M.G. et al. (2013). Liquid exfoliation of layered materials. *Science* 340: 1226419. https://doi.org/10.1126/science.1226419.

131 Eda, G., Yamaguchi, H., Voiry, D. et al. (2011). Photoluminescence from chemically exfoliated MoS_2. *Nano Lett.* 11: 5111–5116. https://doi.org/10.1021/nl201874w.

132 Gordon, R.A., Yang, D., Crozier, E.D. et al. (2002). Structures of exfoliated single layers of WS_2, MoS_2, and $MoSe_2$ in aqueous suspension. *Phys. Rev., B* 65: 125407. https://doi.org/10.1103/PhysRevB.65.125407.

133 Kappera, R., Voiry, D., Yalcin, S.E. et al. (2014). Phase-engineered low-resistance contacts for ultrathin MoS_2 transistors. *Nat. Mater.* 13: 1128–1134. https://doi.org/10.1038/nmat4080.

134 Mittal, M., Sardar, S., and Jana, A. (2021). Chapter 7 - Nanofabrication techniques for semiconductor chemical sensors. In: *Handbook of Nanomaterials for Sensing Applications* (ed. C.M. Hussain and S.K. Kailasa), 119–137. Elsevier.

135 Niu, G., Saint-Girons, G., and Vilquin, B. (2013). Chapter 17 - Epitaxial systems combining oxides and semiconductors. In: *In Molecular Beam Epitaxy* (ed. M. Henini), 451–475. Elsevier.

136 Sun, L., Yuan, G., Gao, L. et al. (2021). Chemical vapour deposition. *Nat. Rev. Methods Primers* 1: 5. https://doi.org/10.1038/s43586-020-00005-y.

137 Huang, J.-K., Pu, J., Hsu, C.-L. et al. (2014). Large-area synthesis of highly crystalline WSe_2 monolayers and device applications. *ACS Nano* 8: 923–930. https://doi.org/10.1021/nn405719x.

138 Najmaei, S., Liu, Z., Zhou, W. et al. (2013). Vapour phase growth and grain boundary structure of molybdenum disulphide atomic layers. *Nat. Mater.* 12: 754–759. https://doi.org/10.1038/nmat3673.

139 van der Zande, A.M., Huang, P.Y., Chenet, D.A. et al. (2013). Grains and grain boundaries in highly crystalline monolayer molybdenum disulphide. *Nat. Mater.* 12: 554–561. https://doi.org/10.1038/nmat3633.

140 Zou, X., Liu, Y., and Yakobson, B.I. (2013). Predicting dislocations and grain boundaries in two-dimensional metal-disulfides from the first principles. *Nano Lett.* 13: 253–258. https://doi.org/10.1021/nl3040042.

141 Dumcenco, D., Ovchinnikov, D., Marinov, K. et al. (2015). Large-area epitaxial monolayer MoS_2. *ACS Nano* 9: 4611–4620. https://doi.org/10.1021/acsnano.5b01281.

142 Chung, J.W., Dai, Z.R., and Ohuchi, F.S. (1998). WS_2 thin films by metal organic chemical vapor deposition. *J. Cryst. Growth* 186: 137–150. https://doi.org/10.1016/S0022-0248(97)00479-X.

143 Dumcenco, D., Ovchinnikov, D., Sanchez, O.L. et al. (2015). Large-area MoS_2 grown using H_2 S as the sulphur source. *2D Materials* 2: 044005. https://doi.org/10.1088/2053-1583/2/4/044005.

144 Eichfeld, S.M., Hossain, L., Lin, Y.-C. et al. (2015). Highly scalable, atomically thin WSe_2 grown via metal–organic chemical vapor deposition. *ACS Nano* 9: 2080–2087. https://doi.org/10.1021/nn5073286.

145 Kang, K., Xie, S., Huang, L. et al. (2015). High-mobility three-atom-thick semiconducting films with wafer-scale homogeneity. *Nature* 520: 656–660. https://doi.org/10.1038/nature14417.

146 Xia, J., Huang, X., Liu, L.-Z. et al. (2014). CVD synthesis of large-area, highly crystalline $MoSe_2$ atomic layers on diverse substrates and application to photodetectors. *Nanoscale* 6: 8949–8955. https://doi.org/10.1039/C4NR02311K.

147 Chang, Y.-H., Zhang, W., Zhu, Y. et al. (2014). Monolayer $MoSe_2$ grown by chemical vapor deposition for fast photodetection. *ACS Nano* 8: 8582–8590. https://doi.org/10.1021/nn503287m.

148 Gao, Y., Liu, Z., Sun, D.-M. et al. (2015). Large-area synthesis of high-quality and uniform monolayer WS_2 on reusable au foils. *Nat. Commun.* 6: 8569. https://doi.org/10.1038/ncomms9569.

149 Kobayashi, Y., Sasaki, S., Mori, S. et al. (2015). Growth and optical properties of high-quality monolayer WS_2 on graphite. *ACS Nano* 9: 4056–4063. https://doi.org/10.1021/acsnano.5b00103.

150 Okada, M., Sawazaki, T., Watanabe, K. et al. (2014). Direct chemical vapor deposition growth of WS_2 atomic layers on hexagonal boron nitride. *ACS Nano* 8: 8273–8277. https://doi.org/10.1021/nn503093k.

151 Tan, H., Fan, Y., Zhou, Y. et al. (2016). Ultrathin 2D photodetectors utilizing chemical vapor deposition grown WS_2 with graphene electrodes. *ACS Nano* 10: 7866–7873. https://doi.org/10.1021/acsnano.6b03722.

152 Zhang, Y., Zhang, Y., Ji, Q. et al. (2013). Controlled growth of high-quality monolayer WS_2 layers on sapphire and imaging its grain boundary. *ACS Nano* 7: 8963–8971. https://doi.org/10.1021/nn403454e.

153 Chen, J., Liu, B., Liu, Y. et al. (2015). Chemical vapor deposition of large-sized hexagonal WSe_2 crystals on dielectric substrates. *Adv. Mater.* 27: 6722–6727. https://doi.org/10.1002/adma.201503446.

154 Liu, B., Fathi, M., Chen, L. et al. (2015). Chemical vapor deposition growth of monolayer WSe_2 with tunable device characteristics and growth mechanism study. *ACS Nano* 9: 6119–6127. https://doi.org/10.1021/acsnano.5b01301.

155 Yoshida, M., Iizuka, T., Saito, Y. et al. (2016). Gate-optimized thermoelectric power factor in ultrathin WSe_2 single crystals. *Nano Lett.* 16: 2061–2065. https://doi.org/10.1021/acs.nanolett.6b00075.

156 Keyshar, K., Gong, Y., Ye, G. et al. (2015). Chemical vapor deposition of monolayer rhenium disulfide (ReS_2). *Adv. Mater.* 27: 4640–4648. https://doi.org/10.1002/adma.201501795.

157 He, X., Liu, F., Hu, P. et al. (2015). Chemical vapor deposition of high-quality and atomically layered ReS_2. *Small* 11: 5423–5429. https://doi.org/10.1002/smll.201501488.

158 Hafeez, M., Gan, L., Li, H. et al. (2016). Large-area bilayer ReS_2 film/multilayer ReS_2 flakes synthesized by chemical vapor deposition for high performance photodetectors. *Adv. Funct. Mater.* 26: 4551–4560. https://doi.org/10.1002/adfm.201601019.

159 Hafeez, M., Gan, L., Li, H. et al. (2016). Chemical vapor deposition synthesis of ultrathin hexagonal $ReSe_2$ flakes for anisotropic Raman property and optoelectronic application. *Adv. Mater.* 28: 8296–8301. https://doi.org/10.1002/adma.201601977.

160 Naylor, C.H., Parkin, W.M., Ping, J. et al. (2016). Monolayer single-crystal 1T′-$MoTe_2$ grown by chemical vapor deposition exhibits weak antilocalization effect. *Nano Lett.* 16: 4297–4304. https://doi.org/10.1021/acs.nanolett.6b01342.

161 Zhou, J., Liu, F., Lin, J. et al. (2017). Large-area and high-quality 2D transition metal telluride. *Adv. Mater.* 29: 1603471. https://doi.org/10.1002/adma.201603471.

162 Joyce, B.A. (1985). Molecular beam epitaxy. *Rep. Prog. Phys.* 48: 1637–1697. https://doi.org/10.1088/0034-4885/48/12/002.

163 Arthur, J.R. (2002). Molecular beam epitaxy. *Surf. Sci.* 500: 189–217. ihttps://doi.org/https:/doi.org/10.1016/S0039-6028(01)01525-4.

164 Ugeda, M.M., Bradley, A.J., Shi, S.-F. et al. (2014). Giant bandgap renormalization and excitonic effects in a monolayer transition metal dichalcogenide semiconductor. *Nat. Mater.* 13: 1091–1095. https://doi.org/10.1038/nmat4061.

165 Barja, S., Wickenburg, S., Liu, Z.-F. et al. (2016). Charge density wave order in 1D mirror twin boundaries of single-layer $MoSe_2$. *Nat. Phys.* 12: 751–756. https://doi.org/10.1038/nphys3730.

166 Vishwanath, S., Liu, X., Rouvimov, S. et al. (2015). Comprehensive structural and optical characterization of MBE grown $MoSe_2$ on graphite, CaF_2 and graphene. *2D Materials* 2: 024007. https://doi.org/10.1088/2053-1583/2/2/024007.

167 Aretouli, K.E., Tsoutsou, D., Tsipas, P. et al. (2016). Epitaxial 2D $SnSe_2$/2D WSe_2 van der Waals heterostructures. *ACS Appl. Mater. Interfaces* 8: 23222–23229. https://doi.org/10.1021/acsami.6b02933.

168 Xenogiannopoulou, E., Tsipas, P., Aretouli, K.E. et al. (2015). High-quality, large-area $MoSe_2$ and $MoSe_2$/Bi_2Se_3 heterostructures on AlN(0001)/Si(111) substrates by molecular beam epitaxy. *Nanoscale* 7: 7896–7905. https://doi.org/10.1039/C4NR06874B.

169 Zhao, W., Ribeiro, R.M., and Eda, G. (2015). Electronic structure and optical signatures of semiconducting transition metal dichalcogenide nanosheets. *Acc. Chem. Res.* 48: 91–99. https://doi.org/10.1021/ar500303m.

170 Mueller, T. and Malic, E. (2018). Exciton physics and device application of two-dimensional transition metal dichalcogenide semiconductors. *npj 2D Mater. Appl.* 2: 29. https://doi.org/10.1038/s41699-018-0074-2.

171 Nagler, P., Plechinger, G., Ballottin, M.V. et al. (2017). Interlayer exciton dynamics in a dichalcogenide monolayer heterostructure. *2D Materials* 4: 025112. https://doi.org/10.1088/2053-1583/aa7352.

172 He, K., Kumar, N., Zhao, L. et al. (2014). Tightly bound excitons in monolayer WSe_2. *Phys. Rev. Lett.* 113: 026803. https://doi.org/10.1103/PhysRevLett.113.026803.

173 Mak, K.F., He, K., Shan, J., and Heinz, T.F. (2012). Control of valley polarization in monolayer MoS_2 by optical helicity. *Nat. Nanotechnol.* 7: 494–498. https://doi.org/10.1038/nnano.2012.96.

174 Jones, A.M., Yu, H., Ghimire, N.J. et al. (2013). Optical generation of excitonic valley coherence in monolayer WSe_2. *Nat. Nanotechnol.* 8: 634–638. https://doi.org/10.1038/nnano.2013.151.

175 Kim, J., Hong, X., Jin, C. et al. (2014). Ultrafast generation of pseudo-magnetic field for valley excitons in WSe_2 monolayers. *Science* 346: 1205–1208. https://doi.org/10.1126/science.1258122.

176 Sie, E.J., McIver, J.W., Lee, Y.-H. et al. (2015). Valley-selective optical stark effect in monolayer WS_2. *Nat. Mater.* 14: 290–294. https://doi.org/10.1038/nmat4156.

177 Mai, C., Semenov, Y.G., Barrette, A. et al. (2014). Exciton valley relaxation in a single layer of WS_2 measured by ultrafast spectroscopy. *Phys. Rev., B* 90: 041414. https://doi.org/10.1103/PhysRevB.90.041414.

178 Wang, G., Bouet, L., Lagarde, D. et al. (2014). Valley dynamics probed through charged and neutral exciton emission in monolayer WSe_2. *Phys. Rev., B* 90: 075413. https://doi.org/10.1103/PhysRevB.90.075413.

179 Tonndorf, P., Schmidt, R., Schneider, R. et al. (2015). Single-photon emission from localized excitons in an atomically thin semiconductor. *Optica* 2: 347–352. https://doi.org/10.1364/OPTICA.2.000347.

180 Srivastava, A., Sidler, M., Allain, A.V. et al. (2015). Optically active quantum dots in monolayer WSe_2. *Nat. Nanotechnol.* 10: 491–496. https://doi.org/10.1038/nnano.2015.60.

181 He, Y.-M., Clark, G., Schaibley, J.R. et al. (2015). Single quantum emitters in monolayer semiconductors. *Nat. Nanotechnol.* 10: 497–502. https://doi.org/10.1038/nnano.2015.75.

182 Koperski, M., Nogajewski, K., Arora, A. et al. (2015). Single photon emitters in exfoliated WSe_2 structures. *Nat. Nanotechnol.* 10: 503–506. https://doi.org/10.1038/nnano.2015.67.

183 Chakraborty, C., Kinnischtzke, L., Goodfellow, K.M. et al. (2015). Voltage-controlled quantum light from an atomically thin semiconductor. *Nat. Nanotechnol.* 10: 507–511. https://doi.org/10.1038/nnano.2015.79.

184 Geim, A.K. and Grigorieva, I.V. (2013). Van der Waals heterostructures. *Nature* 499: 419–425. https://doi.org/10.1038/nature12385.

185 Fang, H., Battaglia, C., Carraro, C. et al. (2014). Strong interlayer coupling in van der Waals heterostructures built from single-layer chalcogenides. *Proc. Natl. Acad. Sci.* 111: 6198–6202. https://doi.org/10.1073/pnas.1405435111.

186 Rivera, P., Schaibley, J.R., Jones, A.M. et al. (2015). Observation of long-lived interlayer excitons in monolayer $MoSe_2$–WSe_2 heterostructures. *Nat. Commun.* 6: 6242. https://doi.org/10.1038/ncomms7242.

187 Baranowski, M., Surrente, A., Klopotowski, L. et al. (2017). Probing the interlayer exciton physics in a $MoS_2/MoSe_2/MoS_2$ van der Waals heterostructure. *Nano Lett.* 17: 6360–6365. https://doi.org/10.1021/acs.nanolett.7b03184.

188 Fogler, M.M., Butov, L.V., and Novoselov, K.S. (2014). High-temperature superfluidity with indirect excitons in van der Waals heterostructures. *Nat. Commun.* 5: 4555. https://doi.org/10.1038/ncomms5555.

189 Yu, Y., Hu, S., Su, L. et al. (2015). Equally efficient interlayer exciton relaxation and improved absorption in epitaxial and nonepitaxial MoS_2/WS_2 heterostructures. *Nano Lett.* 15: 486–491. https://doi.org/10.1021/nl5038177.

190 Gao, S., Yang, L., and Spataru, C.D. (2017). Interlayer coupling and gate-tunable excitons in transition metal dichalcogenide heterostructures. *Nano Lett.* 17: 7809–7813. https://doi.org/10.1021/acs.nanolett.7b04021.

191 Hanbicki, A.T., Chuang, H.-J., Rosenberger, M.R. et al. (2018). Double indirect interlayer exciton in a $MoSe_2/WSe_2$ van der Waals heterostructure. *ACS Nano* 12: 4719–4726. https://doi.org/10.1021/acsnano.8b01369.

192 Fujiwara, H. (2007). *Spectroscopic Ellipsometry: Principles and Applications*. Wiley.

193 Li, D., Song, X., Xu, J. et al. (2017). Optical properties of thickness-controlled MoS_2 thin films studied by spectroscopic ellipsometry. *Appl. Surf. Sci.* 421: 884–890. https://doi.org/10.1016/j.apsusc.2016.09.069.

194 Carvalho, A., Ribeiro, R.M., and Castro Neto, A.H. (2013). Band nesting and the optical response of two-dimensional semiconducting transition metal dichalcogenides. *Phys. Rev., B* 88: 115205. https://doi.org/10.1103/PhysRevB.88.115205.

195 Kumar, R., Carvalho, A., Amara, K.K. et al. (2014). Photocarrier relaxation pathway in two-dimensional semiconducting transition metal dichalcogenides. *Nat. Commun.* 5: 4543. https://doi.org/10.1038/ncomms5543.

196 Zhao, W., Ghorannevis, Z., Chu, L. et al. (2013). Evolution of electronic structure in atomically thin sheets of WS_2 and WSe_2. *ACS Nano* 7: 791–797. https://doi.org/10.1021/nn305275h.

197 Yin, X., Tang, C.S., Wu, D. et al. (2019). Unraveling high-yield phase-transition dynamics in transition metal dichalcogenides on metallic substrates. *Adv. Sci.* 6: 1802093. https://doi.org/10.1002/advs.201802093.

198 Zhang, X., Qiao, X.-F., Shi, W. et al. (2015). Phonon and Raman scattering of two-dimensional transition metal dichalcogenides from monolayer, multilayer to bulk material. *Chem. Soc. Rev.* 44: 2757–2785. https://doi.org/10.1039/C4CS00282B.

199 Kolobov, A.V. and Tominaga, J. (2016). *Two-Dimensional Transition-Metal Dichalcogenides*, 1e. Springer International Publishing: Imprint: Springer.

200 Sandoval, S.J., Yang, D., Frindt, R.F., and Irwin, J.C. (1991). Raman study and lattice dynamics of single molecular layers of MoS_2. *Phys. Rev., B* 44: 3955–3962. https://doi.org/10.1103/PhysRevB.44.3955.

201 Zhao, Y., Luo, X., Li, H. et al. (2013). Interlayer breathing and shear modes in few-trilayer MoS_2 and WSe_2. *Nano Lett.* 13: 1007–1015. https://doi.org/10.1021/nl304169w.

202 Verble, J.L. and Wieting, T.J. (1970). Lattice mode degeneracy in Mo$_2$ and other layer compounds. *Phys. Rev. Lett.* 25: 362–365. https://doi.org/10.1103/PhysRevLett.25.362.

203 Bromley, R.A. (1971). The lattice vibrations of the MoS_2 structure. *Philos. Mag. A* 23: 1417–1427. https://doi.org/10.1080/14786437108217011.

204 Yuan, P., Li, C., Xu, S. et al. (2017). Interfacial thermal conductance between few to tens of layered-MoS_2 and c-Si: effect of MoS_2 thickness. *Acta Mater.* 122: 152–165. https://doi.org/10.1016/j.actamat.2016.09.045.

205 Bertrand, P.A. (1991). Surface-phonon dispersion of MoS_2. *Phys. Rev., B* 44: 5745–5749. https://doi.org/10.1103/PhysRevB.44.5745.

206 Wieting, T.J. and Verble, J.L. (1972). Interlayer bonding and the lattice vibrations of beta-GaSe. *Phys. Rev., B* 5: 1473–1479. https://doi.org/10.1103/PhysRevB.5.1473.

207 Tongay, S., Zhou, J., Ataca, C. et al. (2012). Thermally driven crossover from indirect toward direct bandgap in 2D semiconductors: $MoSe_2$ versus MoS_2. *Nano Lett.* 12: 5576–5580. https://doi.org/10.1021/nl302584w.

208 Tonndorf, P., Schmidt, R., Böttger, P. et al. (2013). Photoluminescence emission and Raman response of monolayer MoS_2, $MoSe_2$, and WSe_2. *Opt. Express* 21: 4908–4916. https://doi.org/10.1364/OE.21.004908.

209 Gutiérrez, H.R., Perea-López, N., Elías, A.L. et al. (2013). Extraordinary room-temperature photoluminescence in triangular WS_2 monolayers. *Nano Lett.* 13: 3447–3454. https://doi.org/10.1021/nl3026357.

210 Zhao, W., Ghorannevis, Z., Amara, K.K. et al. (2013). Lattice dynamics in mono- and few-layer sheets of WS_2 and WSe_2. *Nanoscale* 5: 9677–9683. https://doi.org/10.1039/C3NR03052K.

211 Li, H., Lu, G., Wang, Y. et al. (2013). Mechanical exfoliation and characterization of single- and few-layer nanosheets of WSe_2, TaS_2, and $TaSe_2$. *Small* 9: 1974–1981. https://doi.org/10.1002/smll.201202919.

212 Lee, J.E., Ahn, G., Shim, J. et al. (2012). Optical separation of mechanical strain from charge doping in graphene. *Nat. Commun.* 3: 1024. https://doi.org/10.1038/ncomms2022.

213 Chakraborty, B., Bera, A., Muthu, D.V.S. et al. (2012). Symmetry-dependent phonon renormalization in monolayer MoS_2 transistor. *Phys. Rev., B* 85: 161403. https://doi.org/10.1103/PhysRevB.85.161403.

214 Rice, C., Young, R.J., Zan, R. et al. (2013). Raman-scattering measurements and first-principles calculations of strain-induced phonon shifts in monolayer MoS_2. *Phys. Rev., B* 87: 081307. https://doi.org/10.1103/PhysRevB.87.081307.

215 Hui, Y.Y., Liu, X., Jie, W. et al. (2013). Exceptional tunability of band energy in a compressively strained trilayer MoS_2 sheet. *ACS Nano* 7: 7126–7131. https://doi.org/10.1021/nn4024834.

216 Liu, Z., Amani, M., Najmaei, S. et al. (2014). Strain and structure heterogeneity in MoS_2 atomic layers grown by chemical vapour deposition. *Nat. Commun.* 5: 5246. https://doi.org/10.1038/ncomms6246.

217 Mignuzzi, S., Pollard, A.J., Bonini, N. et al. (2015). Effect of disorder on Raman scattering of single-layer Mo_2. *Phys. Rev., B* 91: 195411. https://doi.org/10.1103/PhysRevB.91.195411.

218 Song, S., Keum, D.H., Cho, S. et al. (2016). Room temperature semiconductor–metal transition of $MoTe_2$ thin films engineered by strain. *Nano Lett.* 16: 188–193. https://doi.org/10.1021/acs.nanolett.5b03481.

219 Kang, J., Liu, W., Sarkar, D. et al. (2014). Computational study of metal contacts to monolayer transition-metal dichalcogenide semiconductors. *Phys. Rev. X* 4: 031005. https://doi.org/10.1103/PhysRevX.4.031005.

220 Popov, I., Seifert, G., and Tománek, D. (2012). Designing electrical contacts to MoS_2 monolayers: a computational study. *Phys. Rev. Lett.* 108: 156802. https://doi.org/10.1103/PhysRevLett.108.156802.

221 Kang, Y., Najmaei, S., Liu, Z. et al. (2014). Plasmonic hot electron induced structural phase transition in a MoS_2 monolayer. *Adv. Mater.* 26: 6467–6471. https://doi.org/10.1002/adma.201401802.

222 Nayak, A.P., Pandey, T., Voiry, D. et al. (2015). Pressure-dependent optical and vibrational properties of monolayer molybdenum disulfide. *Nano Lett.* 15: 346–353. https://doi.org/10.1021/nl5036397.

223 Tan, S.J.R., Abdelwahab, I., Ding, Z. et al. (2017). Chemical stabilization of 1T′ phase transition metal dichalcogenides with giant optical Kerr nonlinearity. *J. Am. Chem. Soc.* 139: 2504–2511. https://doi.org/10.1021/jacs.6b13238.

224 Wilson, N.R., Nguyen, P.V., Seyler, K. et al. Determination of band offsets, hybridization, and exciton binding in 2D semiconductor heterostructures. *Sci. Adv.* 3: e1601832. https://doi.org/10.1126/sciadv.1601832.

225 Yang, H., Liang, A., Chen, C. et al. (2018). Visualizing electronic structures of quantum materials by angle-resolved photoemission spectroscopy. *Nat. Rev. Mater.* 3: 341–353. https://doi.org/10.1038/s41578-018-0047-2.

226 Yuan, H., Liu, Z., Xu, G. et al. (2016). Evolution of the valley position in bulk transition-metal chalcogenides and their monolayer limit. *Nano Lett.* 16: 4738–4745. https://doi.org/10.1021/acs.nanolett.5b05107.

227 Mo, S.-K. (2017). Angle-resolved photoemission spectroscopy for the study of two-dimensional materials. *Nano Convergence* 4: 6. https://doi.org/10.1186/s40580-017-0100-7.

228 Alidoust, N., Bian, G., Xu, S.-Y. et al. (2014). Observation of monolayer valence band spin-orbit effect and induced quantum well states in MoX_2. *Nat. Commun.* 5: 4673. https://doi.org/10.1038/ncomms5673.

229 Riley, J.M., Mazzola, F., Dendzik, M. et al. (2014). Direct observation of spin-polarized bulk bands in an inversion-symmetric semiconductor. *Nat. Phys.* 10: 835–839. https://doi.org/10.1038/nphys3105.

230 Suzuki, R., Sakano, M., Zhang, Y.J. et al. (2014). Valley-dependent spin polarization in bulk MoS_2 with broken inversion symmetry. *Nat. Nanotechnol.* 9: 611–617. https://doi.org/10.1038/nnano.2014.148.

231 Razzoli, E., Jaouen, T., Mottas, M.L. et al. (2017). Selective probing of hidden spin-polarized states in inversion-symmetric bulk MoS_2. *Phys. Rev. Lett.* 118: 086402. https://doi.org/10.1103/PhysRevLett.118.086402.

232 Pierucci, D., Henck, H., Avila, J. et al. (2016). Band alignment and minigaps in monolayer MoS_2-graphene van der Waals heterostructures. *Nano Lett.* 16: 4054–4061. https://doi.org/10.1021/acs.nanolett.6b00609.

233 Ulstrup, S., Koch, R.J., Singh, S. et al. Direct observation of minibands in a twisted graphene/WS_2 bilayer. *Sci. Adv.* 6: eaay6104. https://doi.org/10.1126/sciadv.aay6104.

234 Cao, Y., Fatemi, V., Fang, S. et al. (2018). Unconventional superconductivity in magic-angle graphene superlattices. *Nature* 556: 43–50. https://doi.org/10.1038/nature26160.

235 Wang, L., Shih, E.-M., Ghiotto, A. et al. (2020). Correlated electronic phases in twisted bilayer transition metal dichalcogenides. *Nat. Mater.* 19: 861–866. https://doi.org/10.1038/s41563-020-0708-6.

236 Ghiotto, A., Shih, E.-M., Pereira, G.S.S.G. et al. (2021). Quantum criticality in twisted transition metal dichalcogenides. *Nature* 597: 345–349. https://doi.org/10.1038/s41586-021-03815-6.

237 Pei, D., Wang, B., Zhou, Z. et al. (2022). Observation of gamma-valley moiré bands and emergent hexagonal lattice in twisted transition metal dichalcogenides. *Phys. Rev. X* 12: 021065. https://doi.org/10.1103/PhysRevX.12.021065.

238 Ganguli, S.C., Vaňo, V., Kezilebieke, S. et al. (2022). Confinement-engineered superconductor to correlated-insulator transition in a van der Waals monolayer. *Nano Lett.* 22: 1845–1850. https://doi.org/10.1021/acs.nanolett.1c03491.

239 Kusmartseva, A.F., Sipos, B., Berger, H. et al. (2009). Pressure induced superconductivity in pristine 1T−$TiSe_2$. *Phys. Rev. Lett.* 103: 236401. https://doi.org/10.1103/PhysRevLett.103.236401.

240 Wei, M.J., Lu, W.J., Xiao, R.C. et al. (2017). Manipulating charge density wave order in monolayer 1T−$TiSe_2$ by strain and charge doping: a first-principles investigation. *Phys. Rev., B* 96: 165404. https://doi.org/10.1103/PhysRevB.96.165404.

241 Yokota, K.-i, Kurata, G., Matsui, T., and Fukuyama, H. (2000). Superconductivity in the quasi-two-dimensional conductor 2H-$TaSe_2$. *Physica B* 284–288: 551–552. https://doi.org/10.1016/S0921-4526(99)02166-3.

242 Terashima, K., Sato, T., Komatsu, H. et al. (2003). Charge-density wave transition of 1T−VSe_2 studied by angle-resolved photoemission spectroscopy. *Phys. Rev., B* 68: 155108. https://doi.org/10.1103/PhysRevB.68.155108.

243 Li, Y.W., Jiang, J., Yang, H.F. et al. (2018). Folded superstructure and degeneracy-enhanced band gap in the weak-coupling charge density wave system 2H−$TaSe_2$. *Phys. Rev., B* 97: 115118. https://doi.org/10.1103/PhysRevB.97.115118.

244 Rahn, D.J., Hellmann, S., Kalläne, M. et al. (2012). Gaps and kinks in the electronic structure of the superconductor 2H-$NbSe_2$ from angle-resolved photoemission at 1 K. *Phys. Rev., B* 85: 224532. https://doi.org/10.1103/PhysRevB.85.224532.

245 Ugeda, M.M., Bradley, A.J., Zhang, Y. et al. (2016). Characterization of collective ground states in single-layer $NbSe_2$. *Nat. Phys.* 12: 92–97. https://doi.org/10.1038/nphys3527.

246 Nakata, Y., Sugawara, K., Ichinokura, S. et al. (2018). Anisotropic band splitting in monolayer $NbSe_2$: implications for superconductivity and charge density wave. *Npj 2D Mater. Appl.* 2: 12. https://doi.org/10.1038/s41699-018-0057-3.

247 Calandra, M., Mazin, I.I., and Mauri, F. (2009). Effect of dimensionality on the charge-density wave in few-layer 2H-$NbSe_2$. *Phys. Rev., B* 80: 241108. https://doi.org/10.1103/PhysRevB.80.241108.

248 Chen, P., Chan, Y.H., Fang, X.Y. et al. (2015). Charge density wave transition in single-layer titanium diselenide. *Nat. Commun.* 6: 8943. https://doi.org/10.1038/ncomms9943.

249 Zhang, C., Johnson, A., Hsu, C.-L. et al. (2014). Direct imaging of band profile in single layer MoS_2 on graphite: quasiparticle energy gap, metallic edge states, and edge band bending. *Nano Lett.* 14: 2443–2447. https://doi.org/10.1021/nl501133c.

250 Chiu, M.-H., Zhang, C., Shiu, H.-W. et al. (2015). Determination of band alignment in the single-layer MoS_2/WSe_2 heterojunction. *Nat. Commun.* 6: 7666. https://doi.org/10.1038/ncomms8666.

251 Liu, H., Jiao, L., Yang, F. et al. (2014). Dense network of one-dimensional midgap metallic modes in monolayer $MoSe_2$ and their spatial undulations. *Phys. Rev. Lett.* 113: 066105. https://doi.org/10.1103/PhysRevLett.113.066105.

252 Lezama, I.G., Ubaldini, A., Longobardi, M. et al. (2014). Surface transport and band gap structure of exfoliated 2H-$MoTe_2$ crystals. *2D Materials* 1: 021002. https://doi.org/10.1088/2053-1583/1/2/021002.

253 Yankowitz, M., McKenzie, D., and LeRoy, B.J. (2015). Local spectroscopic characterization of spin and layer polarization in WSe_2. *Phys. Rev. Lett.* 115: 136803. https://doi.org/10.1103/PhysRevLett.115.136803.

254 Sørensen, S.G., Füchtbauer, H.G., Tuxen, A.K. et al. (2014). Structure and electronic properties of in situ synthesized single-layer MoS_2 on a gold surface. *ACS Nano* 8: 6788–6796. https://doi.org/10.1021/nn502812n.

255 Bradley, A.J., Ugeda, M.M., da Jornada, F.H. et al. (2015). Probing the role of interlayer coupling and coulomb interactions on electronic structure in few-layer $MoSe_2$ nanostructures. *Nano Lett.* 15: 2594–2599. https://doi.org/10.1021/acs.nanolett.5b00160.

256 Peng, W., Wang, H., Lu, H. et al. (2021). Recent progress on the scanning tunneling microscopy and spectroscopy study of semiconductor heterojunctions. *Small* 17: 2100655. https://doi.org/10.1002/smll.202100655.

257 Zhang, C., Li, M.-Y., Tersoff, J. et al. (2018). Strain distributions and their influence on electronic structures of WSe_2–MoS_2 laterally strained heterojunctions. *Nat. Nanotechnol.* 13: 152–158. https://doi.org/10.1038/s41565-017-0022-x.

258 Kobayashi, Y., Yoshida, S., Sakurada, R. et al. (2016). Modulation of electrical potential and conductivity in an atomic-layer semiconductor heterojunction. *Sci. Rep.* 6: 31223. https://doi.org/10.1038/srep31223.

259 Duerloo, K.-A.N., Ong, M.T., and Reed, E.J. (2012). Intrinsic piezoelectricity in two-dimensional materials. *J. Phys. Chem. Lett.* 3: 2871–2876. https://doi.org/10.1021/jz3012436.

260 Wu, W., Wang, L., Li, Y. et al. (2014). Piezoelectricity of single-atomic-layer MoS_2 for energy conversion and piezotronics. *Nature* 514: 470–474. https://doi.org/10.1038/nature13792.

261 Zhang, Z., Wang, Y., Watanabe, K. et al. (2020). Flat bands in twisted bilayer transition metal dichalcogenides. *Nat. Phys.* 16: 1093–1096. https://doi.org/10.1038/s41567-020-0958-x.

262 Li, H., Li, S., Naik, M.H. et al. (2021). Imaging moiré flat bands in three-dimensional reconstructed WSe_2/WS_2 superlattices. *Nat. Mater.* 20: 945–950. https://doi.org/10.1038/s41563-021-00923-6.

263 Shabani, S., Halbertal, D., Wu, W. et al. (2021). Deep moiré potentials in twisted transition metal dichalcogenide bilayers. *Nat. Phys.* 17: 720–725. https://doi.org/10.1038/s41567-021-01174-7.

264 Nieken, R., Roche, A., Mahdikhanysarvejahany, F. et al. (2022). Direct STM measurements of R-type and H-type twisted $MoSe_2/WSe_2$. *APL Mater.* 10: 031107. https://doi.org/10.1063/5.0084358.

265 Liu, Y., Qiu, Z., Carvalho, A. et al. (2017). Gate-tunable giant stark effect in few-layer black phosphorus. *Nano Lett.* 17: 1970–1977. https://doi.org/10.1021/acs.nanolett.6b05381.

266 Song, Z., Schultz, T., Ding, Z. et al. (2017). Electronic properties of a 1D intrinsic/p-doped heterojunction in a 2D transition metal dichalcogenide semiconductor. *ACS Nano* 11: 9128–9135. https://doi.org/10.1021/acsnano.7b03953.

267 Blades, W.H., Frady, N.J., Litwin, P.M. et al. (2020). Thermally induced defects on WSe_2. *J. Phys. Chem., C* 124: 15337–15346. https://doi.org/10.1021/acs.jpcc.0c04440.

268 Biadala, L., Peng, W., Lambert, Y. et al. (2019). Trap-free heterostructure of PbS nanoplatelets on InP(001) by chemical epitaxy. *ACS Nano* 13: 1961–1967. https://doi.org/10.1021/acsnano.8b08413.

269 Cheng, F., Hu, Z., Xu, H. et al. (2019). Interface engineering of Au(111) for the growth of 1T′-$MoSe_2$. *ACS Nano* 13: 2316–2323. https://doi.org/10.1021/acsnano.8b09054.

270 Lu, J., Bao, D.-L., Qian, K. et al. (2017). Identifying and visualizing the edge terminations of single-layer $MoSe_2$ island epitaxially grown on Au(111). *ACS Nano* 11: 1689–1695. https://doi.org/10.1021/acsnano.6b07512.

271 Lauritsen, J.V., Nyberg, M., Vang, R.T. et al. (2003). Chemistry of one-dimensional metallic edge states in MoS_2 nanoclusters. *Nanotechnology* 14: 385–389. https://doi.org/10.1088/0957-4484/14/3/306.

272 Bollinger, M.V., Lauritsen, J.V., Jacobsen, K.W. et al. (2001). One-dimensional metallic edge states in MoS_2. *Phys. Rev. Lett.* 87: 196803. https://doi.org/10.1103/PhysRevLett.87.196803.

273 Kang, S., Lee, D., Kim, J. et al. (2020). 2D semiconducting materials for electronic and optoelectronic applications: potential and challenge. *2D Materials* 7: 022003. https://doi.org/10.1088/2053-1583/ab6267.

274 Chen, Y.-C., Cao, T., Chen, C. et al. (2015). Molecular bandgap engineering of bottom-up synthesized graphene nanoribbon heterojunctions. *Nat. Nanotechnol.* 10: 156–160. https://doi.org/10.1038/nnano.2014.307.

275 Rizzo, D.J., Wu, M., Tsai, H.-Z. et al. (2019). Length-dependent evolution of type II heterojunctions in bottom-up-synthesized graphene nanoribbons. *Nano Lett.* 19: 3221–3228. https://doi.org/10.1021/acs.nanolett.9b00758.